Improving structural build-up of limestone-calcined clay-cement pastes by using inorganic additives

Chen, Yu; Zhang, Yu; He, Shan; Liang, Xuhui; Schlangen, Erik; Çopuroğlu, Oğuzhan

DOI
10.1016/j.conbuildmat.2023.131959

Publication date
2023

Document Version
Final published version

Published in
Construction and Building Materials

Construction and Building Materials 392 (2023) 131959

Contents lists available at ScienceDirect

Construction and Building Materials

journal homepage: www.elsevier.com/locate/conbuildmat

Improving structural build-up of limestone-calcined clay-cement pastes by using inorganic additives

Yu Chen *, Yu Zhang, Shan He, Xuhui Liang, Erik Schlangen, Oğuzhan Çopuroğlu

Microlab, Faculty of Civil Engineering and Geosciences, Delft University of Technology, Delft, The Netherlands

ARTICLE INFO

Keywords:
Limestone-calcined clay-cement
Rheology
Structural build-up
Very early-age hydration
$CaCl_2$
Gypsum
3D concrete printing

ABSTRACT

In 3D concrete printing, fast structuration is a prerequisite for ideal buildability. This paper aims to study the impact of inorganic additives, i.e., $CaCl_2$ and gypsum, on structural build-up and very early-age hydration of limestone-calcined clay-cement (LC3) pastes within the first 70–80 min. Results show that, increasing the dosage of $CaCl_2$ or gypsum can accelerate storage modulus G' and static yield stress evolution with time, as well as increase chemically bound water (H) content and total specific surface area (SSA_{total}). Furthermore, good correlations were found between G' and H content, as well as static yield stress and the ratio of free water content to SSA_{total}. The acceleration by $CaCl_2$ can be attributed to stimulating C_3S and C_3A hydration and promoting crystal formation, i.e., ettringite, portlandite, and Friedel's salt. Additionally, the increase in gypsum percentage led to a large amount of unreacted gypsum in the system, resulting in an increase in SSA_{total}.

1. Introduction

Limestone-calcined clay-cement (LC3), being one of the most promising sustainable cements, has attracted significant interest from academia and industry [1–3]. Compared to common supplementary cementitious materials (SCMs), such as blast furnace slag, fly ash and silica fume, which are being depleted [3], calcined clay appears to be an ideal sustainable alternative to SCMs. Some of the advantages of using calcined clay can be listed as: (1) clay deposits are abundant worldwide [1,3]; (2) relatively low CO_2 is emitted during the calcination [3,4]; (3) calcined clay is rich in reactive alumina and silica [5]. Furthermore, as a cement substitution, the combination of calcined clay and limestone brings many benefits, including the enhanced ultimate mechanical and durability-related performance of hardened concrete and a significant decrease in CO_2 footprint [1,3,6,7]. Also, calcined clay is an appropriate resource to develop novel construction materials. For example, LC3 has been successfully employed as a sustainable cementitious binder for extrusion-based 3D concrete printing (see [8–10]). 3D printable LC3-based mixtures with less than 300 kg/m^3 of ordinary Portland cement (OPC) are proposed by Chen et al. [11]. Owing to its layered crystal structure, high specific surface area and water absorption, calcined clay is considered a favorable ingredient to enhance the thixotropy of fresh cementitious materials [12,13]. Compared to typical OPC pastes, LC3 pastes exhibit a higher thixotropic index and structuration rate, as reported by [13,14]. However, relying solely on the high thixotropy nature of calcined clay might not be sufficient to achieve the desired buildability in 3D concrete printing. Additional chemical additives, e.g., viscosity modifying agents, or setting accelerators, may still be required, especially to reach the goal of set-on-demand printing as described by [15,16].

$CaCl_2$, as one of the most efficient setting accelerators [17], can be used to achieve the fast structuration of fresh cementitious materials. Many researchers [18–22] have used $CaCl_2$ to compensate for the slow structural build-up and hydration, as well as to improve the low early-age strength of high volume SCMs (fly ash and slag) blended cements. Although helpful in compensating hydration rate deficiencies, use of $CaCl_2$ is not allowed in reinforced concrete designs due to posing early corrosion risk of steel reinforcement. On the other hand, steel rebar is not typically employed in 3D printed cementitious materials, although recent developments show that it is technically possible [23,24]. Besides, there has been considerable interest towards using polymeric fibers and fiber-reinforced polymer (FRP) composites to improve the toughness and ductility of concrete (see [25,26]). Furthermore, as reported by [18,27], the corrosion potential is lower in slag blended cements due to the high chloride binding capacity of reactive aluminate phases in slag. Compared to slag, calcined clay (especially metakaolin)

* Corresponding author.
E-mail addresses: Y.Chen-6@tudelft.nl (Y. Chen), Y.Zhang-28@tudelft.nl (Y. Zhang), S.He-2@tudelft.nl (S. He), X.Liang-1@tudelft.nl (X. Liang), Erik.Schlangen@tudelft.nl (E. Schlangen), O.Copuroglu@tudelft.nl (O. Çopuroğlu).

https://doi.org/10.1016/j.conbuildmat.2023.131959
Received 16 July 2022; Received in revised form 10 May 2023; Accepted 25 May 2023
Available online 2 June 2023

Table 1
Oxide compositions of calcined clay, limestone powder, and Portland cement.

XRF [wt.%]	Calcined clay	Limestone powder	Portland cement
CaO	0.55	55.40	68.71
SiO_2	55.14	0.17	17.41
Al_2O_3	38.43	0.03	4.62
Fe_2O_3	2.60	0.04	2.75
K_2O	0.17	0	0.63
TiO_2	1.12	0	0.34
ZrO_2	0.05	0	0
SO_3	0	0	2.44
Other	1.94	44.36	3.10
Total	100.00	100.00	100.00

with a higher content of reactive alumina appears to show a better chloride binding capacity according to [5,28–30]. However, up to now, far too little attention has been paid to employing $CaCl_2$ as an accelerator in limestone-calcined clay-based cementitious materials. Similarly, the influence of $CaCl_2$ on rheology, structuration, and hydration of LC3 pastes is underexplored.

Gypsum, hemihydrate, or anhydrite needs to be added to LC3 to delay the aluminate reaction peak occurrence and improve the early-age strength [2,6,31]. As reported by [2,31–33], 1–3% of additional gypsum can be used in LC3 if the clinker is sourced from OPC. However, the additional gypsum will not lead to severe expansion since the total sulfate content (wt.% of the binder mass) is still below the threshold of 5–6% (depending on the original gypsum content in the OPC used) [31]. In the case of commercial LC3-50, as mentioned by Scrivener et al. [3], 5% of gypsum is directly mixed with 50% clinker, 15% limestone, and 30% calcined clay at the cement production stage. Moreover, Hay et al. [6] reported that the additions of gypsum or hemihydrate could also mitigate the autogenous shrinkage of LC3 pastes, probably due to the massive formation of ettringites. For OPC, gypsum is added to retard aluminate compounds (C_3A, C_4AF) hydration, resulting in an acceleration of silicate hydration. Nevertheless, if the amount of calcium sulfate is disproportionately higher than the aluminate ions, large crystals of gypsum will rapidly be precipitated, leading to a severe loss of consistency, which is known as “false set” [34]. This effect may also significantly influence the rheology and early-age hydration characteristics of LC3 pastes. So far, however, there has been little study about the impact of gypsum addition on the structural build-up of LC3 pastes.

With the increased interest and development of extrusion-based 3D concrete printing (3DCP), there is an urgent need to better characterize and understand structural build-up of fresh cementitious materials. This is because formwork is eliminated in the layer-wise construction process

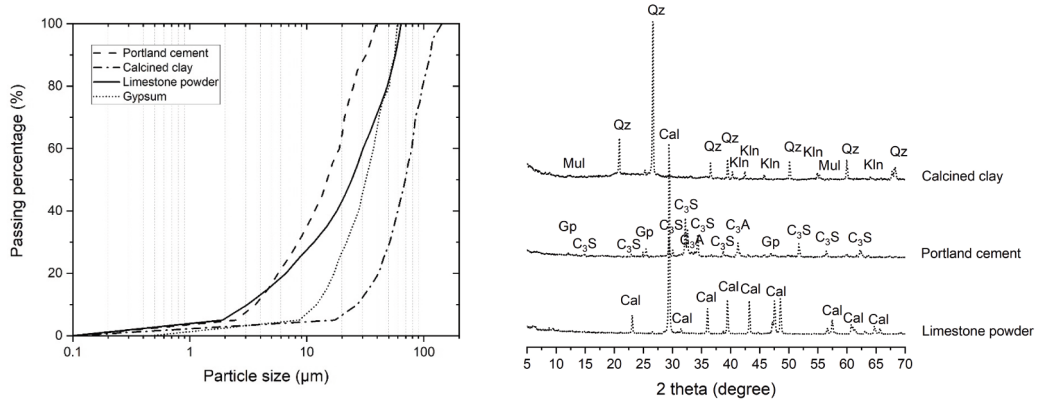

Fig. 1. (a) Particle size distribution of calcined clay, limestone powder, Portland cement, and gypsum; (b) X-ray diffraction (Cu-Kα radiation) patterns of calcined clay, limestone powder, and Portland cement, adapted from [9]. Cal-calcite, Gp-gypsum, C_3S-alite, C_3A-tricalcium aluminate, Mul-mullite, Qz-quartz, Kln-kaolinite.

Table 2
Physical characteristics of calcined clay, limestone powder, Portland cement, and gypsum.

	Calcined clay	Limestone powder	Portland cement	Gypsum
Density [g/cm^3]	2.51	2.65	3.12	2.32
SSA [m^2/g]	10.06	1.22	1.16	0.53
D_{v50} [μm]	69.35	24.19	14.86	31.94

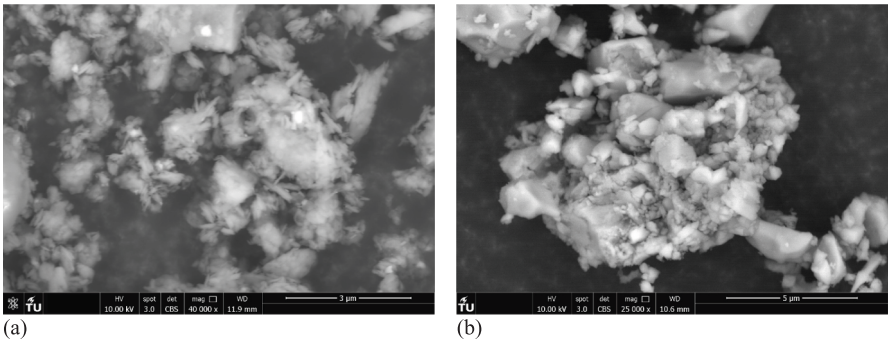

Fig. 2. Electron micrograph of (a) calcined clay and (b) limestone powder under secondary electron imaging mode.

of 3DCP [12,35]. Therefore, the deposited layer must exhibit sufficiently high strength not only to retain the shape of one layer but also to withstand the dead weight of the subsequent layers [9,36]. The shape stability of a single layer is linked to thixotropy and, more particularly, to the static yield stress of fresh cementitious material [36]. In this context, thixotropy is only defined as a reversible effect, i.e., the viscosity of fresh cementitious material (originally at rest) reduces with increasing shear force (de-flocculation) and then recovers in time as the shear force decreases (flocculation) [37–39]. Roussel [40] explained thixotropic behavior of fresh cement pastes from a microstructural point of view. The macroscopic reversible effect is related to the breakage and reconstruction of C-S-H bridges between cementitious particles. When the applied shear stress is insufficient to break the bridges induced by the continuous progression of hydration with time, the irreversible effect is expected. As the main reason for workability loss, hydration plays a dominant role in influencing this irreversible effect [38]. In order to prevent the plastic deformation or even elastic buckling of the printed structure, the deposited layer needs to evolve its stiffness within a short time (tens of minutes) [41,42]. Structuration or structural build-up is used to describe the development of stiffness over time in this context.

To quantify the structural build-up of fresh cementitious materials, two rheological approaches should be considered, i.e., characterizations of elasticity (through oscillations) and yield stress (through flow-onset) evolution with time [12,41]. The elasticity, stiffening and very early-age hydration of fresh cement paste are usually probed by small amplitude oscillatory shear (SAOS) test [37,43–45]. The increase in storage modulus *G'* acquired from SAOS testing indicates the growth of C-S-H bridges and nucleation. Compared to the quantification of elasticity evolution (SAOS test) that requires an expensive and sensitive device [46], static yield stress measurement is a more practical and common method to assess structural build-up of fresh cementitious materials, especially for printable mixtures (see [45,47–50]). However, static yield stress is dominated by the overlapping effect of colloidal interaction, direct contact, and C-S-H bridges [41]. Thus, it is suggested to quantify both elasticity and static yield stress to better assess the structural build-up of fresh cementitious materials. According to the literature, static yield stress can be measured using different test protocols, e.g., constant shear rate [37,38,51,52], stress growth [53], and creep recovery [53–55]. Among them, applying a constant shear rate protocol seems to be the commonly agreed method to determine the static yield stress of fresh cementitious materials.

This paper aims to investigate the effect of inorganic additives, i.e., gypsum and $CaCl_2$, on the structural build-up and very early-age hydration of LC3 pastes during a short time (70–80 min). To this end, two experimental approaches were organized, the first of which characterized the structuration of LC3 pastes using rheometry. The structural build-up of fresh paste samples was quantified by static yield stress measurement (constant shear rate protocol) and SAOS test. Secondly, isothermal calorimetry, total specific surface area measurement, thermogravimetric and qualitative X-ray Diffraction analysis were conducted to assess phase assemblages in the studied materials. Finally, indicators and influencing factors of structural build-up, correlations between structuration and hydration, as well as plausible mechanisms related to the observed phenomena are discussed.

2. Material and methods

2.1. Materials

The solid components used in this work were CEM I 52.5 Portland cement (PC), calcined clay (CC), limestone powder (LP), and gypsum. CC that contained about 50% of metakaolin was purchased from Argeco, France. According to our earlier study [11], the reactive aluminate in CC is about 32 wt%. Gypsum with more than 99% purity was provided by Merck KGaA, Germany. Oxide compositions obtained by X-ray fluorescence (XRF) spectrometry of PC, CC, and LP are given in Table 1. Fig. 1 (a) illustrates particle size distribution (obtained by laser diffractometry) of PC, CC, LP and gypsum. X-ray diffraction (XRD) patterns of PC, CC and LP are demonstrated in Fig. 1 (b). A PhilipsPW1830 powder X-ray diffractometer with Cu-Kα radiation operated at 45 kV and 40 mA was employed to obtain XRD patterns. It can be found that the main impurity of CC was quartz. CC displayed the largest average particle size (D_v50) compared to other dry components, owing to the quartz impurity. Table 2 summarizes the physical characteristics, i.e., density, Brunauer-Emmett-Teller (BET) specific surface area (SSA), and D_v50, of all binding materials. CC exhibited a much higher SSA than other fines. The particle morphology of CC and LP was observed under secondary electron (SE) mode of scanning electron microscopy (SEM). As shown in Fig. 2, both CC and LP particles showed clustered structures. A subhedral flaky habit was found in CC particles, which may be the main cause of the high SSA. In contrast, LP particles displayed granular and rhombohedral crystal habits.

Table 3 shows the mixture compositions of the LC3 pastes. In all mixtures, the binder mainly comprised PC (50 wt% of the binder) and the blend of CC and LP in a mass ratio of 2:1. For mixtures N1 and N2, CC and LP possessed 50 wt% of the binder. Gypsum was used to replace 2 wt % of CC and LP in mixtures S1, S2 and S3, and 4 wt% in mixture R. 2.4–5 wt% of commercial accelerator solution with 33 wt% $CaCl_2$ concentration (Cugla, Netherlands) was added in mixtures N2, S2, and S3. After mixing $CaCl_2$ solution with water, a constant water-to-binder ratio (W/B) of 0.3 was achieved for all studied mixtures. Additionally, a polycarboxylate ether (PCE)-based superplasticizer (SP) (MasterGlenium®51, BASF, Netherlands) was used in all mixtures at 0.6 wt% of the binder. All fresh pastes were prepared by following the mixing procedures shown in Table 4. Time zero (t = 0 min) was defined as the moment of mixing liquid with dry components.

The physical features, including liquid volume fraction (ϕ_{total}), packing density (φ_m), and water film thickness (WFT_0) of the studied mixtures are presented in Table 5. In cementitious materials, a fraction of the mixing water occupies the intergranular voids. The remaining excess water forms a water film layer around the grains. The thickness of the water film layer influences the rheology of fresh mixtures [56,57]. According to earlier studies [57–59], the water film thickness (*WFT*) of fresh pastes can be computed by using the following equations:

$$WFT = \frac{\phi_{excess}}{SSA_0} \tag{1}$$

$$\phi_{excess} = \phi_{total} - \phi_{void} \tag{2}$$

$$\phi_{void} = \frac{1-\varphi_m}{\varphi_m} \tag{3}$$

where ϕ_{excess}, ϕ_{total} and ϕ_{void} represent the excess water volume fraction, the water ratio of the paste and void ratio, respectively. φ_m is the packing density of all cementitious pastes measured using the Puntke test (see details in [60,61]). The mixing liquid, including water and 2 wt% SP (0.6 wt% of the binder), was employed in the Puntke test. SSA_0 is the total specific surface area of studied mixtures. As shown in Table 5, all paste mixtures display similar values of ϕ_{total}, φ_m, and WFT_0, Therefore, 2–4 wt% gypsum addition would not distinctly modify the physical characteristics of the studied mixtures at t = 0 min.

2.2. Test procedures

2.2.1. Rheological tests

The rheological characteristics of the studied mixtures were determined using an Anton Paar MCR 302e rheometer. A four-blade vane geometry (diameter: 22 mm; height: 40 mm) in a cylindrical measuring cup (inner diameter: 28.92 mm; depth: 68 mm.) was employed to perform the rheological tests. The inner surface of the measuring cup was equipped with steel lamellas to avoid slippage. After preparation, about 85 g of fresh paste was filled in the measuring cell using a spoon.

Table 3
Mixture composition of cementitious materials (wt.% of the total dry components).

	Portland cement	Calcined clay	Limestone powder	Gypsum	Water	$CaCl_2$ solution*	Superplasticizer
N1	50	33	17	0	30	0	0.6
N2	50	33	17	0	28.4	2.4	0.6
S1	50	32	16	2	30	0	0.6
S2	50	32	16	2	28.4	2.4	0.6
S3	50	32	16	2	27	5	0.6
R	50	30.7	15.3	4	30	0	0.6

$CaCl_2$ solution*: 33% $CaCl_2$ concentration.

Table 4
Instructions for the mixing protocol for fresh paste preparation.

Time [min: s]	Instructions
−3:00	Homogenize dry blends. Mix at low speed using a HOBART planetary mixer.
0:00	Add liquid (water + SP) during mixing.
2:00	Stop, scrape the wall and bottom of the bowl by hand.
2:30	Mix at high speed.
4:00	Stop, start experiments.

Table 5
Liquid volume fraction, packing density, and water film thickness of studied mixtures.

	Liquid volume fraction (ϕ_{total}). [vol.%]	Packing density (φ_m). [vol.%]	Water film thickness (WFT_0) at t = 0 min. [μm]
N1	46.2	58.7	0.013
N2	46.2	58.7	0.013
S1	46.2	58.9	0.014
S2	46.2	58.9	0.014
S3	46.2	58.9	0.014
R	46.1	58.6	0.014

Prior to the test, a fresh sample was compacted on a vibration table at a 30 Hz frequency for 10 s to reduce the amount of air bubbles. All rheological tests were conducted under a constant temperature at 21 ± 1 °C. The following subsections present the details of the test protocols adopted.

2.2.1.1. Hysteresis loop and static yield stress tests. To ensure the same flow/shear history, the fresh paste at the material age of 7 min was pre-sheared at 100 s^{-1} for 30 s, followed by a resting time of 150 s. A hysteresis loop test was then performed at 10 min following the moment of liquid addition (water + SP). The test procedure was identical to an earlier study [62]. The applied shear rate increased linearly from 0 s^{-1} to 100 s^{-1} for 30 s, and it was kept at 100 s^{-1} for 60 s. Afterward, a linear ramp-down shear rate from 100 s^{-1} to 0 s^{-1} was applied in 30 s. As shown in Fig. 3 (a), the acquired descending curve from this test was used to fit Bingham model (Eq (4)) for obtaining dynamic yield stress τ_d and plastic viscosity μ_p at the material age of 10 min.

$$\tau = \tau_d + \mu_p \dot{\gamma} \tag{4}$$

where τ and $\dot{\gamma}$ represent shear stress and shear rate. Conducting the hysteresis loop test can also ensure a deflocculated state of fresh paste [38,62] before the static yield stress measurement.

After waiting for 180 s, the constant shear rate (CSR) – single sample approach (see [62,63]) was performed at the material age of 15 min, 30 min, 45 min, 60 min, and 75 min. This test may be terminated earlier if the measured torque of the tested material exceeds the Rheometer limit (the maximum torque: 230 mN·m). For CSR – single sample approach, it is recommended to set a constant applied shear rate and duration time to ensure a constant applied shear strain (deformation). Since the rigidity and stiffness of printable cementitious materials are significantly higher than flowable cementitious materials, using a slow shear rate (in the range of 0.001–0.01 s^{-1}) with a long test duration seems not to be suitable in this context [12,37,62]. After trial–error processes, a constant shear rate of 0.24 s^{-1} and 20 s duration time were executed in the current work, resulting in an applied shear strain of 4.8 unit. Fig. 3 (b) presents a typical curve of the current CSR test. It can be found that the shear stress increases to a peak value (flow onset) and then gradually decreases to a relatively stable value. The peak value is referred to the static yield stress at the specific material age. Please note that the obtained static yield stress in a single sample measurement may be smaller

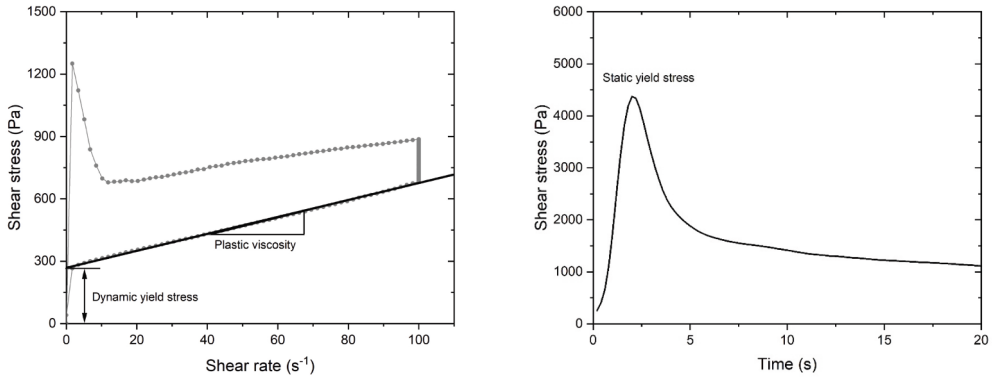

Fig. 3. Typical curves of (a) hysteresis loop test – the descending curve is fitted by Bingham model and (b) CSR test.

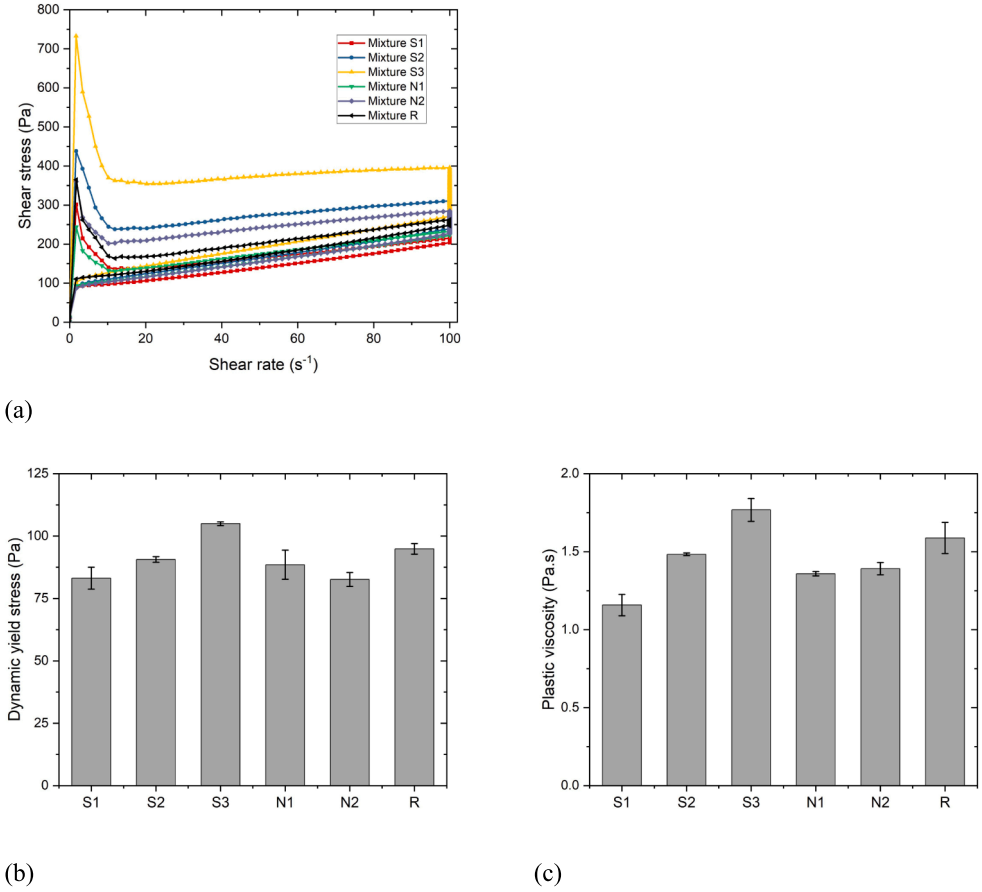

Fig. 4. (a) Hysteresis loop curves of different mixtures at 10 min; (b) Dynamic yield stress and (c) plastic viscosity obtained by fitting Bingham model. The R-squared value of all linear fitted curves is more than 0.90.

than that of a multi-sample measurement due to the destructive nature of the CSR protocol. Nevertheless, the objective of this study was to compare the effect of different chemical additives on the yield stress evolution with time instead of acquiring the "exact" value.

2.2.1.2. Small amplitude oscillatory shear test. SAOS test, as a non-destructive test, was used to investigate the structuration (elasticity, stiffening, and hydration evolution with time) of different fresh pastes. A continuous sinusoidal excitation (which results in a controlled strain of usually 0.01%–0.001% for cementitious materials [37,64]) was applied to the sample over time, and the material response (complex modulus G^*) that can be converted to storage modulus (G') and loss modulus (G'') was measured.

$$G^* = G' + iG'' \tag{5}$$

where i is imaginary unit. As the in-phase and elastic component of the response, the evolution of G' can be used to indicate the elasticity development of fresh sample over time. In contrast, G'' represents the out-of-phase and viscous component of the response, and it relates to the dissipated energy in each test cycle [12,41]. The ratio between G' and G'' is defined as the loss factor that is also an indicator to illustrate the structure network development of fresh cementitious materials with time [65]. It is worth noting that G' remains independent when the applied strain is within the linear viscoelastic domain (LVED) [41,43]. Thus, prior to SAOS test, a strain-sweep test should be conducted to determine the LVED of studied materials. Similar to rheological tests in Section 2.2.1.1., a pre-shear step (shear rate of 100 s^{-1} for 30 s) was performed initially. After a resting time of 30 s, the strain-sweep test with the strain of 0.001% − 50% and a constant frequency of 1 Hz was executed at 8 min. According to the strain-sweep test results (see Section 3.1.2.), a SAOS test was immediately carried out at the strain of 0.005% (which is similar to the applied strain in [37,43,44,65,66]) and a constant frequency of 1 Hz at the material age of 23 ± 1 min. The test duration was 60 min, and the data was collected after each 30 s.

2.2.2. Early-age hydration

2.2.2.1. XRD, TGA and SSA_{total} measurement. Paste samples in rheological tests of Section 2.2.1. were also used for the thermogravimetric analysis (TGA), X-ray diffraction (XRD) analysis, and total specific surface area (SSA_{total}) measurement. The hydration of paste samples was stopped at 30 min and 75 min using solvent exchange method with isopropanol, in accordance with [8,67]. Netzsch STA 449 F3 Jupiter was employed for TGA. For each test, about 50 mg of powder sample was heated from 40 to 900 °C with a heating rate of 10 °C/min. The whole test process was at an argon environment with a 30 ml/min flow rate. XRD patterns of different paste mixtures were determined using a powder X-ray diffractometer, with Cu-Kα radiation operated at 45 kV and 40 mA. The diffraction angle (2θ) is in the range of 5°-70°. For quantifying SSA_{total} of hydrated cementitious materials, dry powders were prepared according to the procedures described in [11,68]. The SSA_{total} of samples at different material ages was measured using a BET multi-point nitrogen physisorption apparatus (Gemini VII 2390).

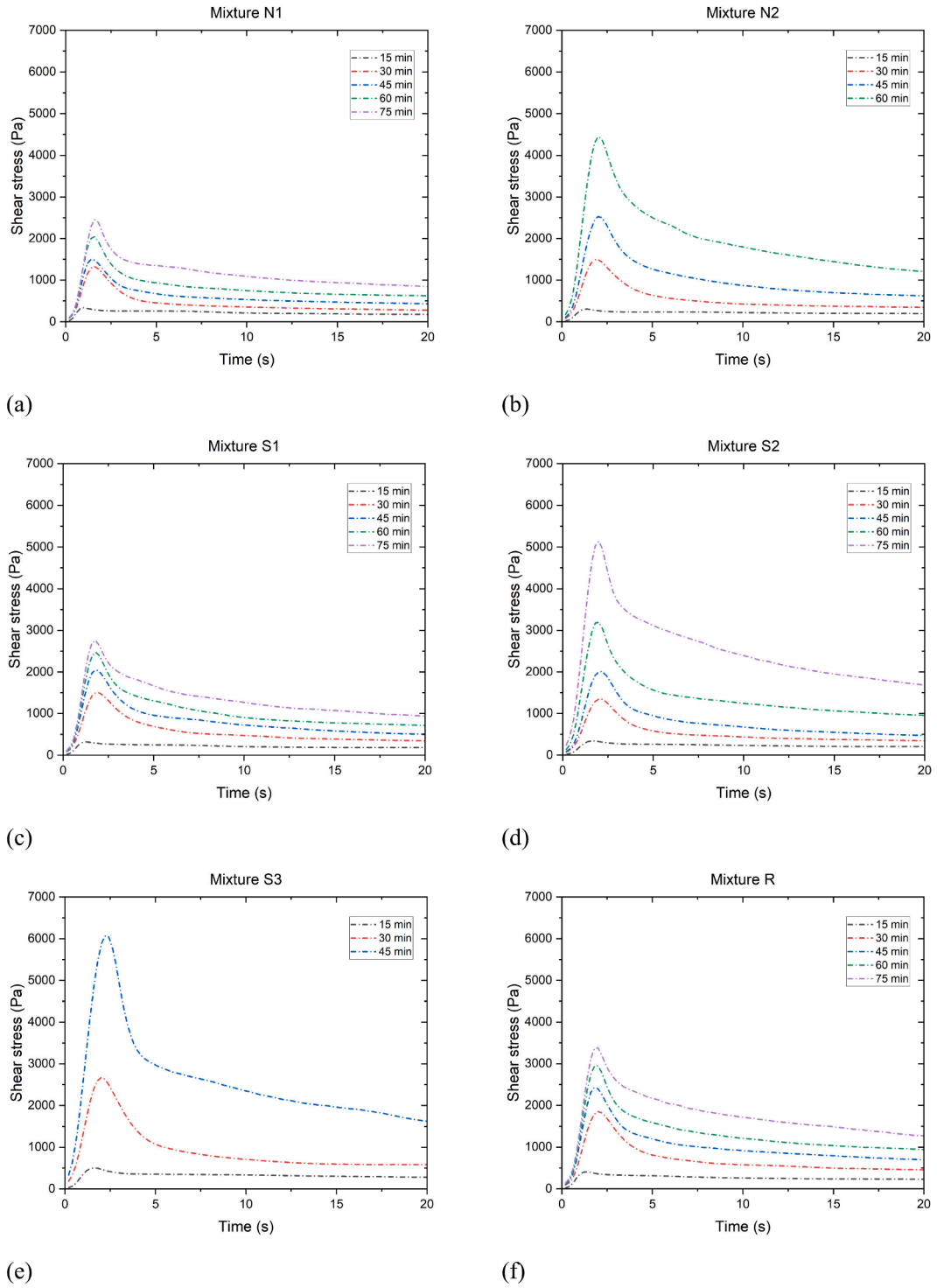

Fig. 5. CSR-single sample test results of (a) mixture N1, (b) mixture N2, (c) mixture S1, (d) mixture S2, (e) mixture S3, (f) mixture R, at 15, 30, 45, 60, and 75 min. Due to the limit of maximum torque (230 mN·m), the static yield stress of mixtures N2 (75 min) and S3 (60 and 75 min) could not be measured via the current approach.

2.2.2.2. Isothermal calorimetry test. Isothermal calorimetry test was conducted by an eight-channel TAM Air isothermal calorimeter to measure the hydration heat released during the first 2 days. The pre-mixed liquid composed of mixing water and SP ($CaCl_2$ solution was also added for mixtures N2, S2 and S3) was poured into the pre-weighed dry components, and then the mixture was stirred by a small mixing machine for 2.5 min. Afterward, 6 g of fresh paste was filled into a 20 ml glass vessel. Together with the reference vessel, the sample vessel was placed in the calorimeter under 20 °C.

3. Results

3.1. Structural build-up of fresh pastes

3.1.1. Yield stress evolution

Fig. 4 (a) displays the hysteresis loop curves of different studied

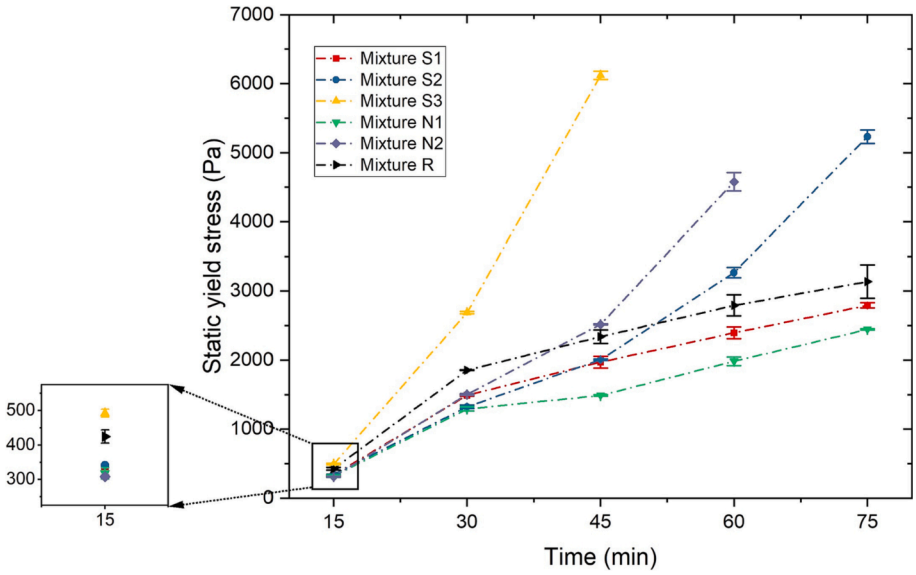

Fig. 6. Static yield stress of different mixtures at various resting times.

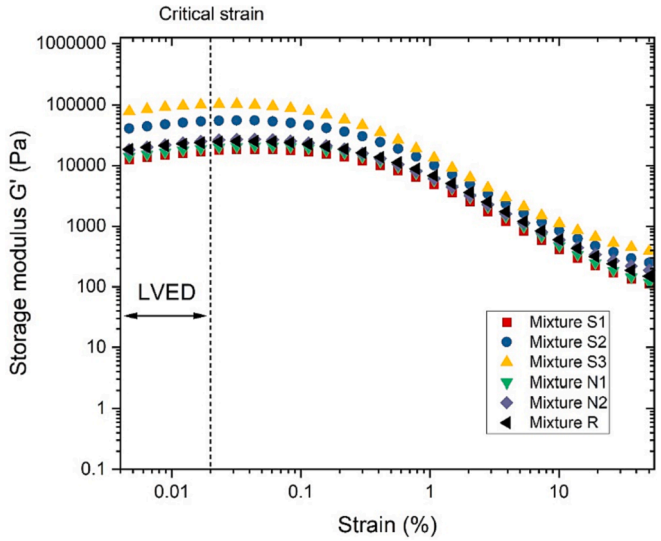

Fig. 7. Strain sweep test results: Linear viscoelastic domain and critical strain of different mixtures at the frequency of 1 Hz.

pastes at the material age of 10 min (test duration: 2 min). All curves show a similar pattern. The descending branch of each curve was fitted using Bingham model to obtain dynamic yield stress and plastic viscosity, which are plotted in Fig. 4 (b) and (c), respectively. For mixtures containing 2 wt% gypsum (S1, S2 and S3), both Bingham values are clearly increased by increasing the dosage of $CaCl_2$. However, such an increase cannot be found in mixtures without gypsum (N1 and N2). The effect of gypsum on flow behaviors can be observed by comparing Bingham values of mixtures N1, S1 and R. As shown in Fig. 4 (b), the dynamic yield stress and plastic viscosity declined with the addition of 2 wt% gypsum and increased with increasing the gypsum content to 4 wt %. However, the investigation of flow behavior is not the main goal of the current study and will not be discussed further.

CSR-single sample test results at different material ages (every 15 min since water addition) are presented in Fig. 5. Please note that the shear stress value was computed using the measured torque, according to [69]. For mixtures N2 and S3, the static yield stress cannot be measured at the resting time of 60 min and 75 min since the maximum torque of the rheometer (230 mN·m) has been reached. As shown in Fig. 5, the shear stress in all curves increases gradually with increasing the test duration until reaching the peak value. Except for the curves at 15 min, the peak value for different mixtures at various ages corresponds to a similar test duration (1.7–2.5 s). In contrast, a slightly shorter test duration time is required for fresh pastes at 15 min. After the stress peak, the shear stress decreases as the test duration approaches an equilibrium value. All shear stress peaks in Fig. 5 were collected and regarded as the static yield stresses.

As illustrated in Fig. 6, mixtures with and without $CaCl_2$ display different development trends. For mixtures S1, N1 and R, the static yield stress exhibits a near-linear increase with time from 30 min. The static yield stress at different material ages is enhanced by increasing the amount of gypsum. Nevertheless, owing to the addition of $CaCl_2$ accelerator, a steep increase of static yield stress with time can be observed for mixtures S2, S3 and N2. For mixtures containing 2 wt% gypsum, the static yield stress at all tested ages is largely increased by adding 5 wt% $CaCl_2$ (mixture S3). The yield stress of mixture S2 with 2.4 wt% $CaCl_2$ solution is higher than that of mixture S1 after 45 min. In contrast, the acceleration of static yield stress induced by the addition of 2.4 wt% $CaCl_2$ solution is more efficient for mixtures without gypsum. Mixture N2 shows much higher static yield stresses after 15 min and 30 min than mixtures N1 and S2, respectively. Except for mixture S3, mixture R has the most elevated static yield stress within the first 30 min compared to others due to the addition of 4 wt% gypsum.

3.1.2. *Critical strain and elasticity evolution*

Fig. 7 shows the strain sweep response of different fresh pastes at the material age of 8 min. It can be found that there are two main regimes for each storage modulus (G') curve: an initial plateau and a descending branch relating to shear-induced microstructure breakage. The initial plateau means the linear viscoelastic domain (LVED) and the end of LVED, where G' starts to decrease with the increase of strain, is defined as the critical strain. As illustrated in Fig. 7, all critical strains are within 0.01–0.1%. Thus, the strain amplitude selected in the SAOS test should be smaller than 0.01% to remain in LVED for all mixtures. This can confirm that the 0.005% strain amplitude employed in the SAOS test is appropriate for the current study.

SAOS test results are presented in Fig. 8. Fig. 8 (a) and (b) show the storage modulus G' development over time of different mixtures on linear and logarithmic scales. For fresh cementitious materials, the evolution of G' value can indicate the particle flocculation and

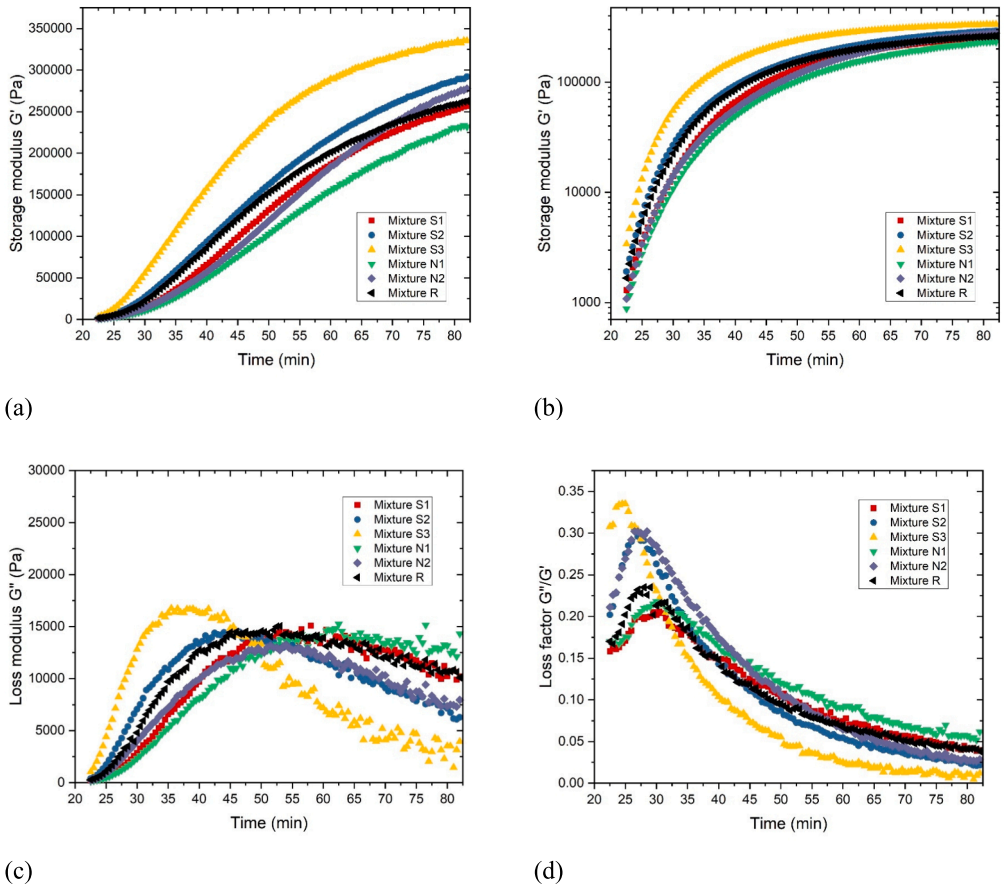

Fig. 8. SAOS test results: (a) Storage modulus *G'* evolution with time – linear scale; (b) Storage modulus *G'* evolution with time – logarithmic scale; (c) Loss modulus *G''* evolution with time; (d) Loss factor evolution with time.

formation of C-S-H bridges between particles due to the very early-age hydration [37,41]. All curves in Fig. 8 (a) exhibit the same curve pattern. Each curve has a near-linear increase regime (see Fig. 9 (a)), which is attributed to forming a percolated network due to particle flocculation [70]. The slope of such a linear regime is defined as the *G'* evolution rate, as demonstrated in Fig. 9 (b). It can be found that mixture S3 displays the highest *G'* value during the test and *G'* evolution rate than others. For mixtures with 2 wt% gypsum (S1, S2 and S3), *G'* is significantly increased by increasing the dosage of $CaCl_2$. Similarly, mixture N2 also shows a faster development of *G'* than mixture N1, especially after 40 min. Mixtures S2 and N2 exhibit a similar *G'* evolution rate that is higher than mixtures S1 and N1. Unlike the static yield stress development in Fig. 6, mixture S2 has a larger *G'* value than that of mixture N2 from 22 min to 82 min. For mixtures N1, S1 and R, increasing the amount of gypsum can promote the *G'* evolution. However, the magnitude difference between mixtures R and S1 in *G'* rapidly decreases from about 50 min.

Fig. 8 (c) and (d) illustrate the evolution of loss modulus *G''* and loss factor of different pastes. Both values increase with time initially and then decrease after reaching a peak. The rising of loss factor means that *G''* grows faster than *G'*. The increase of *G''* represents the growth of viscous behavior of tested materials owing to the lost energy induced by the relative motions between flocculated clusters and/or particles during the shear process [71–73]. This phenomenon can be attributed to the released free water during the condensation stage [65]. At this stage, the water consumption rate seems to be less than the void filling rate caused by the rapid precipitation of hydrates with a large volume. Also, the loss factor peak may be ascribed to the gelation [74]. The loss factor and *G''* peak time (t_1 and t_2) are presented in Fig. 9 (c). The mixture with a high *G'* evolution rate corresponds to a short time to reach the peak value of *G''* and loss factor (see Fig. 9 (d)). After the peak, the loss factor gradually decreases with time (approaching zero), which indicates the formation process of a percolated network. As shown in Fig. 8 (a) and (d), the mixture with a small loss factor displays a large *G'* at 82 min.

3.2. Early-age hydration kinetics

3.2.1. Isothermal calorimetry

The normalized heat flow and cumulative heat of different mixtures by paste weight for 2 days are plotted in Fig. 10 (a) and (c). For mixtures S1, S2 and S3, the intensity and appearance time of the main hydration peak are significantly enhanced and declined by increasing the dosage of $CaCl_2$, as shown in Fig. 10 (a). Also, the cumulative heat value within the first 6 h is increased. Nevertheless, after 6 h, the difference between mixtures S1, S2 and S3 in cumulative heat is gradually reduced. For mixtures without gypsum (N1 and N2), adding 2.4 wt% $CaCl_2$ can accelerate the first-day hydration, whereas the cumulative heat of both mixtures is very similar after 31 h. By increasing the amount of gypsum (from 0 to 4 wt%), both intensity and appeared time of the main hydration peak are not influenced, whereas the aluminate peak is delayed and even transferred as a broad hump in mixture R. Such a phenomenon is consistent with findings from [2,6,31]. With the same $CaCl_2$ dosage, mixture N2 displays a slightly higher and narrower main hydration peak than mixture S2, probably due to the overlap of C_3S and aluminate peaks according to [6,75,76]. Fig. 10 (b) and (d) show the heat flow and cumulative heat of different mixtures from 15 min to 90 min. Note that the

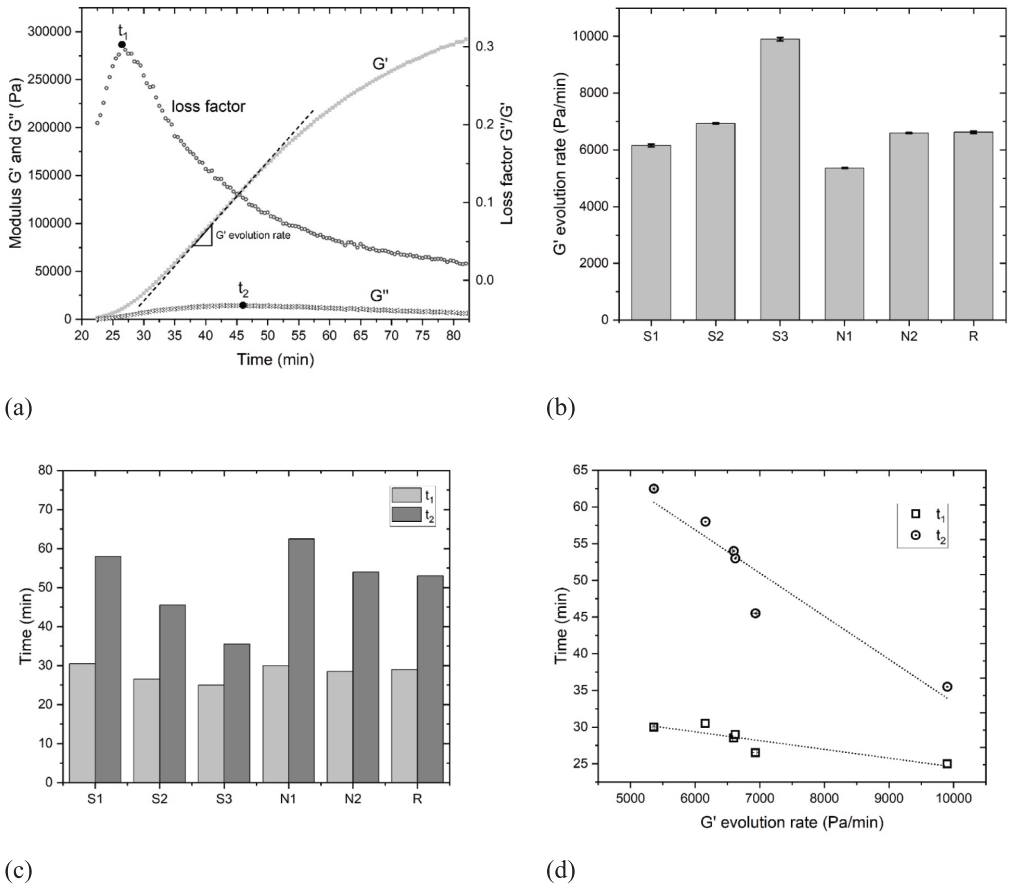

Fig. 9. (a) Example of storage modulus *G'*, loss modulus *G''*, and loss factor acquired from the SAOS test. t_1 and t_2 indicate the peak time of loss factor and *G''*. *G'* evolution rate is the slope of the linear increase regime in the *G'* and time curve. (b) *G'* evolution rate of different mixtures; (c) t_1 and t_2 of different mixtures; (d) Correlation between *G'* evolution rate, and t_1 and t_2.

released heat within the first 15 min was mainly contributed by the particle wetting and initial dissolution, which was removed in Fig. 10 (c) and (d). Within the first 90 min, increasing $CaCl_2$ dosage can significantly increase both heat flow and cumulative heat values. Also, the onset of the acceleration stage in heat flow occurs earlier. In contrast, adding gypsum appears to decrease the heat flow and cumulative heat within the initial 90 min (see mixtures R, S1 and N1), which can be attributed to the reduction of C_3A hydration heat due to the high amount of sulfate available in the system.

3.2.2. TGA, XRD and SSA_{total}

Thermogravimetric (TG) and derivative thermogravimetric (DTG) curves of different mixtures at 30 min and 75 min are presented in Fig. 11 (a) and (b), respectively. A prominent peak (P1) at around 100 °C in all DTG curves is induced by dehydration of ettringite and C-S-H gel layers [77,78]. According to [67,77,78], the peak (P2) appeared at 125–200 °C in DTG curves may be the decomposition peak of gypsum and/or monocarboaluminate (Mc), whereas this peak may also be partially contributed by the mass loss of Friedel's salt for mixtures with $CaCl_2$ addition. The formation of Friedel's salt in mixture S3 is further confirmed by the peak (P3) at 250–350 °C in DTG curves. A slight rise (P4) at about 430 °C (especially for mixture S3) indicates the decomposition of calcium hydroxide (CH). According to Refs [8,67,79], the amount of chemically bound water (H) can be computed by the mass loss during the temperature between 40 °C and 600 °C (see Eq (6)). The CH decomposition temperature is in the range of 400–500 °C. The CH content of different samples was calculated using Eq (7).

$$W_{[H_2O]} = \frac{M_{40^\circ C} - M_{600^\circ C}}{M_{600^\circ C}} \times 100(\%) \tag{6}$$

and

$$W_{[Ca(OH)_2]} = \frac{M_{400^\circ C} - M_{500^\circ C}}{M_{600^\circ C}} \times \frac{m_{[Ca(OH)_2]}}{m_{[H_2O]}} \times 100(\%) \tag{7}$$

where $W_{[H_2O]}$ and $W_{[Ca(OH)_2]}$ are the mass percentages of chemically bound water and calcium hydroxide in mixtures, respectively; $M_{40℃}$, $M_{400℃}$, $M_{500℃}$ and $M_{600℃}$ are the TG results at 40 °C, 400 °C, 500 °C, and 600 °C; $m_{[Ca(OH)_2]}$, and $m_{[H_2O]}$ represent the molar masses of calcium hydroxide (74 g/mol) and water (18 g/mol).

Fig. 11 (c) and (d) demonstrate the computed H and CH contents of different mixtures at 30 min and 75 min, respectively. It can be found that both amounts are increased by increasing the dosage of $CaCl_2$. Compared to mixtures without gypsum (N1 and N2), mixtures S1 and S2 display higher H amounts, which can be partially ascribed to the chemically bound water from the additional gypsum. Note that the chemically bound water from gypsum was not deduced in the current calculation. Due to the high gypsum addition, mixture R exhibits a much higher H content than mixtures N1 and S1 at 30 min. Compared to mixture N2, mixture S2 shows a higher CH content at 75 min.

XRD results do further confirm the crystal phases mentioned in DTG curves. As shown in Fig. 12, ettringite is found in all mixtures at 75 min as the most typical crystal. The intensity of the ettringite peak seems to be enhanced by adding $CaCl_2$ (mixtures S1, S2 and S3 or mixtures N1

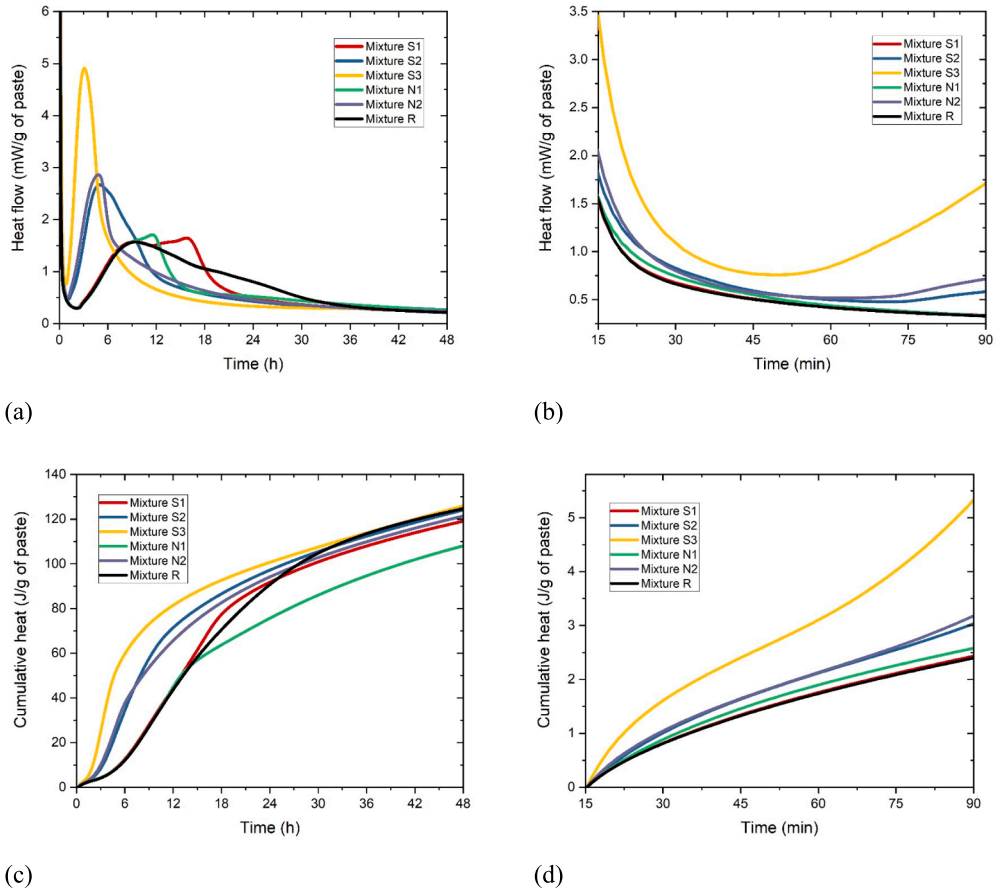

Fig. 10. Isothermal calorimetry test results: (a) Normalized heat flow by weight of paste with time (48 h); (b) Normalized heat flow by weight of paste with time (15–90 min); (c) Normalized cumulative heat by weight of paste with time (48 h); (d) Normalized cumulative heat by weight of paste with time (15–90 min).

and N2), whereas it is not affected by increasing the amount of gypsum. As reported by [70], the rate of ettringite formation does not depend on the amount of gypsum at the beginning. Friedel's salt is present in mixtures N2 and S3 but not in S2. The intensity of the gypsum peak is increased by additional gypsum (mixtures N1, S1 and R). Compared to mixture S2, mixture S3 displays a much lower gypsum peak. 5% $CaCl_2$ addition appears to accelerate gypsum consumption and promote the formation of ettringite and Friedel's salt. Since the position of the Mc peak is very similar to that of gypsum, the intensity of Mc in mixtures with additional gypsum cannot be identified.

Fig. 13 (a) compares the SSA_{total} of paste samples at the material age of 30 min and 75 min. Compared to the $CaCl_2$ addition, gypsum addition plays a more dominant role in the SSA_{total} of paste samples at 30 min. Mixture R with 4% of gypsum shows the highest SSA_{total} than the others. This is probably caused by the promotion of initial ettringite and gypsum precipitation, as reported by [68,70,80]. For mixtures with the same gypsum addition, the mixture with $CaCl_2$ displays a high SSA_{total} at 75 min, whereas the increase of $CaCl_2$% cannot contribute to the rise of SSA_{total} at the beginning (30 min). A similar phenomenon can be found in mixtures N1 and N2. As shown in Fig. 13 (b), the increase rate of SSA_{total} (from 30 min to 75 min) can be significantly boosted by increasing the $CaCl_2$ percentage. Such an increase may be related to the precipitation of Friedel's salt and C-S-H since adding $CaCl_2$ can stimulate the C_3S hydration and formation of Friedel's salt [28,81,82]. For the mixtures without $CaCl_2$, increasing the gypsum dosage can also increase the growth rate of SSA_{total}. However, only a minor difference in the increase rate between mixtures R and S1 can be observed.

4. Discussions

4.1. Indicators and dominant factors of structuration

Static yield stress and elasticity evolution with time were used to quantify the structural build-up ability of fresh LC3 pastes. The storage modulus *G'* obtained from the SAOS test can be regarded as the indicator of elasticity. According to [38,41], the fast linear increase in *G'* is attributed to the colloidal interactions and after the formation of percolated network, the growth of *G'* is tied to the C-S-H nucleation. C-S-H bridges between particles appear to play a dominant role in elastic behavior. In contrast, the static yield stress is defined as the minimum force to initiate the relative motion of particles/flocculated clusters, which arises from the overlap of C-S-H nucleation, colloidal attractions, and solid contact (frictions) between particles/flocculated clusters [41,53]. As shown in Fig. 14, such friction and connection between particles are dominated by the quantities of free water and early-age hydration products (C-S-H and crystal phases). The free water can be temporarily stored in the void between particles (later age: capillary water) and/or the micropores/interlayer of particles (i.e., calcined clays [8,13]), and physically adsorbed on the particle surfaces as lubrication water (later age: gel water and/or interlayer water). As mentioned in Section 2.1, the thickness of the lubrication water layer is defined as *WFT*, which decreases with time due to the hydration. Therefore, as shown in Fig. 15, when comparing different mixtures, higher static yield stress does not necessarily correspond to higher *G'*, which is in good agreement with [41]. Also, note that even for the same mixture, the flow histories in SAOS and CSR tests are different, affecting the correlation

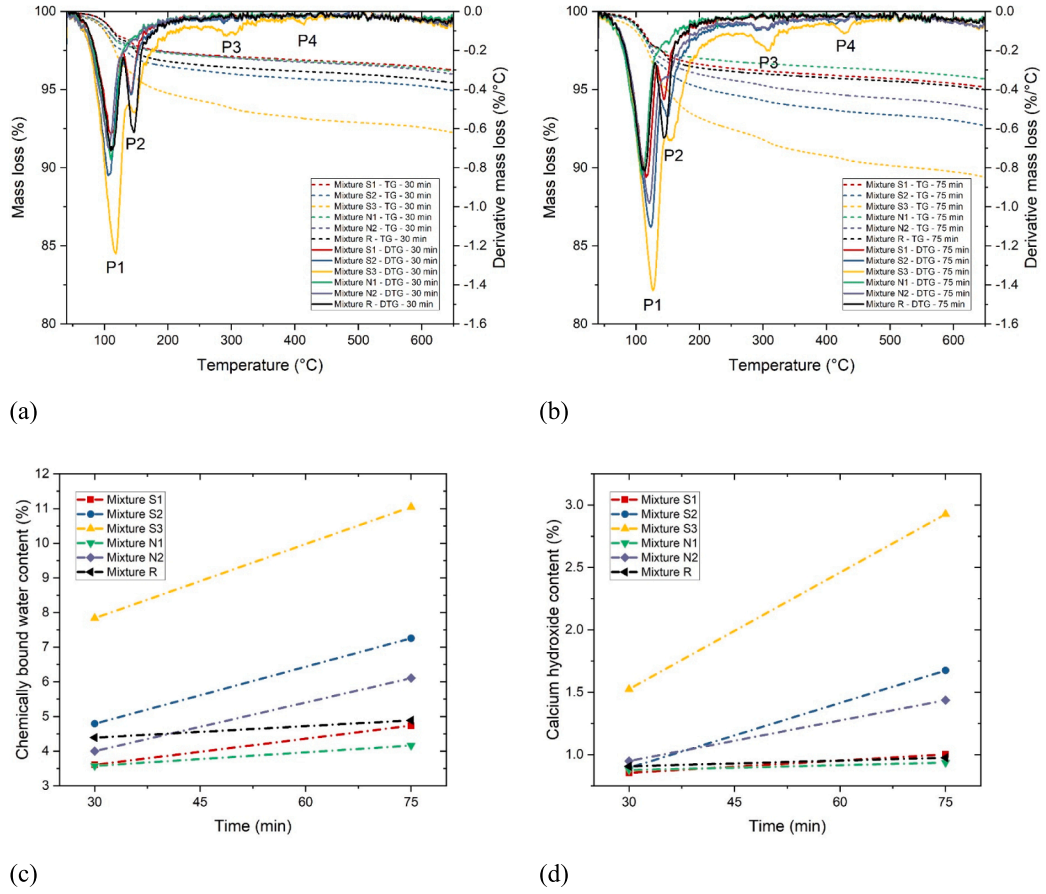

Fig. 11. (a) TG and DTG curves of different mixtures at 30 min; (b) TG and DTG curves of different mixtures at 75 min; (c) The normalized chemically bound water content after 30 min, relative to the dry sample mass at 600 °C; (d) The normalized calcium hydroxide content after 75 min, relative to the dry sample mass at 600 °C. P1: C-S-H and ettringite; P2: Gypsum, monocarboaluminate and/or Friedel's salt; P3: Friedel's salt; P4: Calcium hydroxide.

between *G'* and static yield stress.

H and CH contents at 30 min and 75 min obtained by TGA can indicate the quantities of hydration products. The linear relationship between *G'*, static yield stress, and H, CH contents are presented in Fig. 16. A good correlation between *G'* and H content is found at the same material age in Fig. 16 (a). Higher *G'* indicates more hydration products, which means higher chemically bound water content. However, the increase in H content does not always coincide with the rise in static yield stress at 30 min (Fig. 16 (c)) due to factors, i.e., friction between particles and the thickness of the lubrication water layer. As shown in Fig. 16 (c) and (d), portlandite may not be an ideal indicator for revealing the structuration of fresh pastes due to the limited amount formed at very early ages (except mixture S3). Additionally, the measurement of released heat and SSA_{total} was also employed to characterize the early-age hydration of studied mixtures. Due to the inhibition of gypsum on C_3A hydration, the growth of cumulative heat from isothermal calorimetry cannot fully correspond with the increase in H content, as illustrated in Fig. 17 (a). Furthermore, the correlation between SSA_{total} and H content is relatively weak in Fig. 17 (b). Compared to other mixtures, mixture R with relatively low H contents at 30 min and 75 min exhibits extremely high SSA_{total} values.

It is assumed that the porosity (voids between particles and micropores in the particles, i.e., calcined clay) of all studied mixtures is the same. In that case, *WFT* only depends on the free water amount and SSA_{total}, according to Eqs (1) and (2). The free water content at 30 min and 75 min can be computed based on H content from the TGA. An inversely proportional correlation between *G'*, static yield stress, and the ratio of free water content to SSA_{total} (free water content/SSA_{total}) can be found in Fig. 18. Compared to *G'*, the increase in free water content/SSA_{total} leads to a more significant reduction of static yield stress. This phenomenon confirms the critical role of *WFT* on static yield stress.

4.2. *Effect of $CaCl_2$ and additional gypsum on structuration of LC3 pastes*

Increasing the dosage of $CaCl_2$ can vastly accelerate the structural build-up of LC3 mixtures with or without gypsum within the first 75 min. As shown in Figs. 6 and 8, the mixture with a higher dosage of $CaCl_2$ exhibits a relatively higher value of *G'* and static yield stress (especially after 45 min). The acceleration of structuration induced by $CaCl_2$ is likely due to the enhancement of early-age hydration. Adding $CaCl_2$ can increase the influential ion concentration in pore solution, which appears to play a dominant role in the acceleration of C_3S hydration. Besides, $CaCl_2$ increases not only the rate of structural build-up (Figs. 6 and 8) but also the hydration rate (i.e., the intensity of C_3S peak and slope rate of acceleration stage in isothermal calorimetry), as shown in Fig. 10 (a).

In addition, $CaCl_2$ can also promote the crystal formation of LC3 pastes within the first 75 min. As shown in Fig. 12, except for CH (and/or calcium oxychloride compounds depending on $CaCl_2$ concentration), the formation of ettringite was enhanced by increasing the dosage of $CaCl_2$ at 75 min. Mixtures with high content of ettringites may exhibit relatively high static yield stress due to the needle-like morphology of ettringite. However, the appearance time of massive ettringite precipitation may depend on the $CaCl_2$ concentration. As illustrated in Fig. 6, in

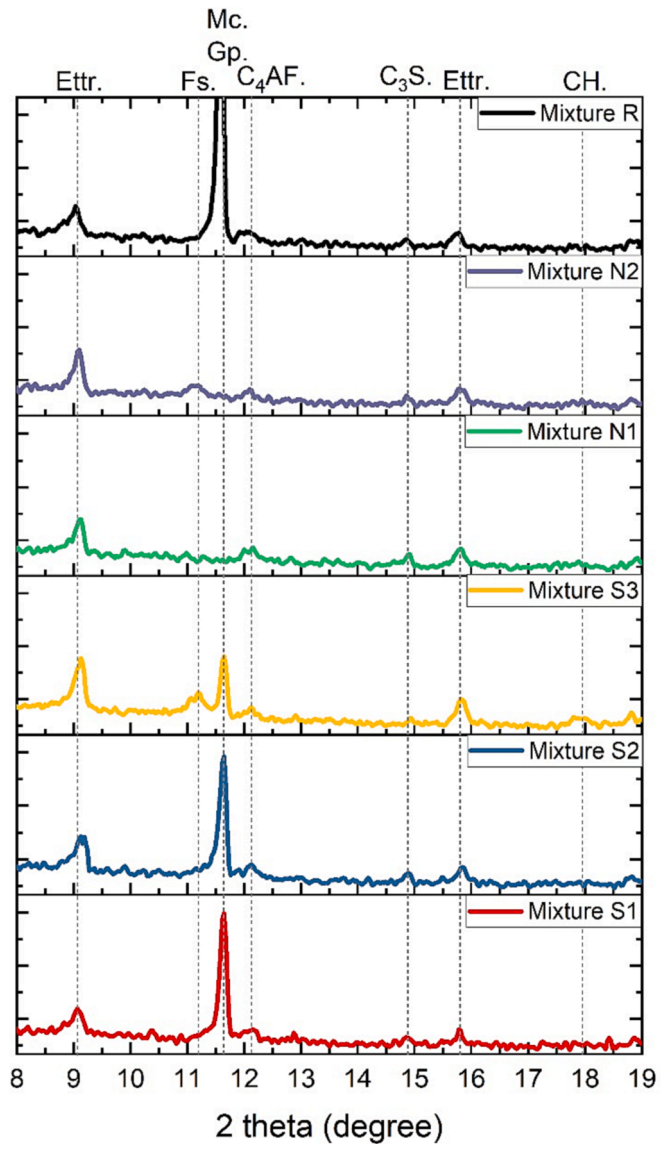

Fig. 12. XRD patterns for different mixtures at 75 min. Ettr. – Ettringite; Fs. – Friedel's salt; Gp. – Gypsum; Mc. – Monocarboaluminate; CH. – Portlandite.

comparison with mixture S1, mixture S2 shows smaller yield stress at 30 min, which agrees with [83]. The authors attributed this initial reduction of yield stress to the delayed ettringite precipitation because of using a small dosage of $CaCl_2$. Nevertheless, such a delay was not an issue at 75 min in the current study, as shown in Figs. 6 and 12. Friedel's salt was observed in mixtures N2 and S3 at 75 min (Fig. 12). The formation of Friedel's salt is related to the reaction between chloride ions and C_3A, C_4AF and/or AFm [5,84,85]. However, Friedel's salt was not found in mixture S2 at 75 min. The presence of additional gypsum in mixture S2 may hinder the formation of Friedel's salt at a very early age, which may be related to the AFm and/or aluminate phases (e.g., C_3A and C_4AF) binding competition between Cl^- and SO_4^{2-} (see [28,86–88]). Such an influence seems to be diminished by increasing the dosage of $CaCl_2$ (in the case of mixture S3). Compared to mixture N2, mixture S2 displays a faster *G'* evolution, a higher value of SSA_{total} and the ratio of free water content to SSA_{total} at the same material age. However, the static yield stress of mixture N2 is higher than mixture S2 within the first 75 min. In this context, Friedel's salt may increase the friction between particles dominating the enhancement of static yield stress.

For the mixtures without $CaCl_2$ (N1, S1, and R), increasing the dosage of gypsum increases the evolution of *G'* (within the first 82 min) and static yield stress (within the first 75 min). As shown in Figs. 16, 17 and 18, the enhancement of structuration by gypsum may be attributed to the increase in chemically bound water content and SSA_{total} as well as the decrease in the ratio of free water content to SSA_{total}. Increasing the gypsum content may slightly promote the very early-age hydration of LC3. Lapeyre and Kumar [89] pointed out that the aluminate ions from metakaolin (main reactive phases in calcined clay) may inhibit the dissolution of C_3S and hinder the growth of C-S-H nuclei. According to [90,91], the inhibition of C_3S dissolution depends on the calcium ions and pH in the pore solution, as aluminate ions interact with the hydroxylated C_3S surface and form ionic bonds with calcium ions of the surface. The additional gypsum in the system may effectively bind the aluminate ions, thereby alleviating the inhibition of C_3S dissolution. Additionally, Zunino and Scrivener [92] reported that the addition of gypsum could enhance the hydration of the pure C_3S phase. However, the mechanism behind this enhancement remains unclear. Furthermore, according to Gauffinet-Garrault [70], the mechanical efficiency of C-S-H can be augmented by increasing the quantity of gypsum (for the alite-C_3A-gypsum system). The author [70] attributed this enhancement to the presence of solid gypsum. In this study, unreacted gypsum was detected in mixtures S1, S2, S3 and R (Fig. 12), which may also correspond to the high value of SSA_{total}, especially at 30 min.

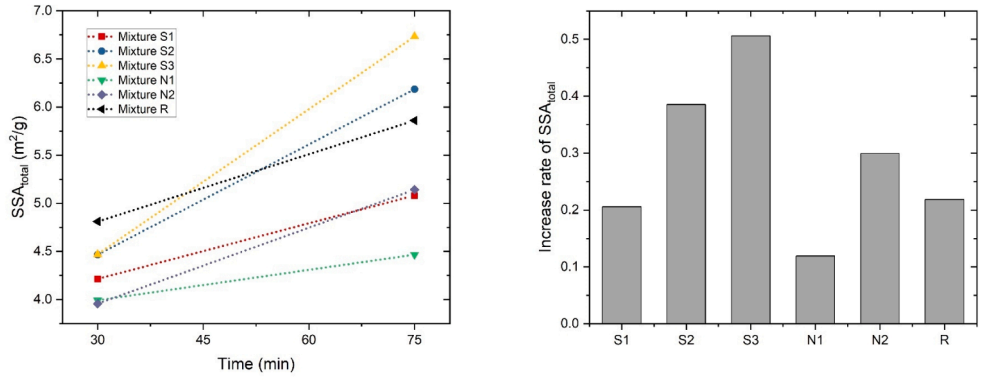

Fig. 13. (a) SSA_{total} of different paste samples at 30 min and 75 min; (b) Increase rate of SSA_{total} of different paste samples between 30 min and 75 min.

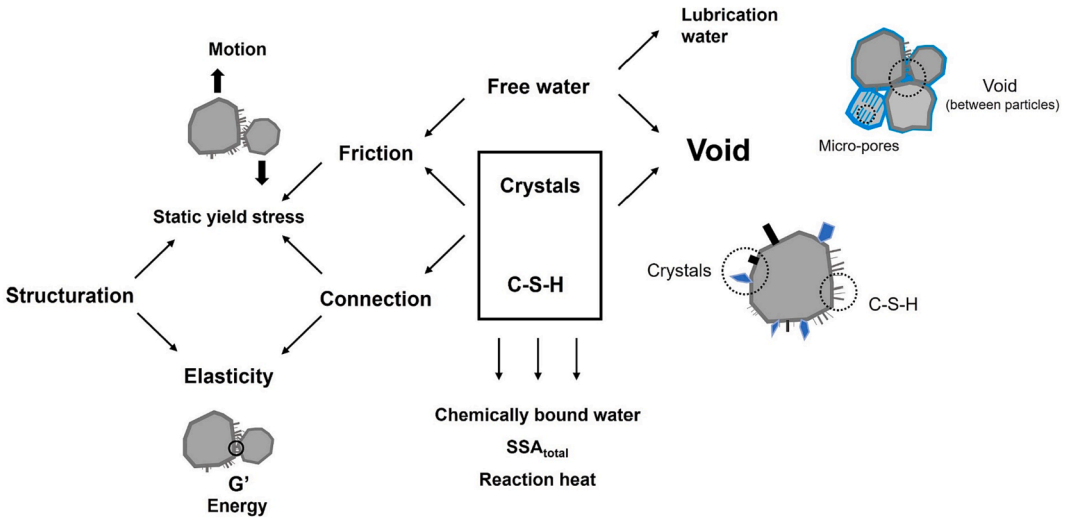

Fig. 14. Illustration of indicators and dominant factors for the structural build-up of cementitious materials. Elasticity represents the particle connection induced by C-S-H nucleation, which can be indicated by the magnitude of *G'* from the SAOS test.

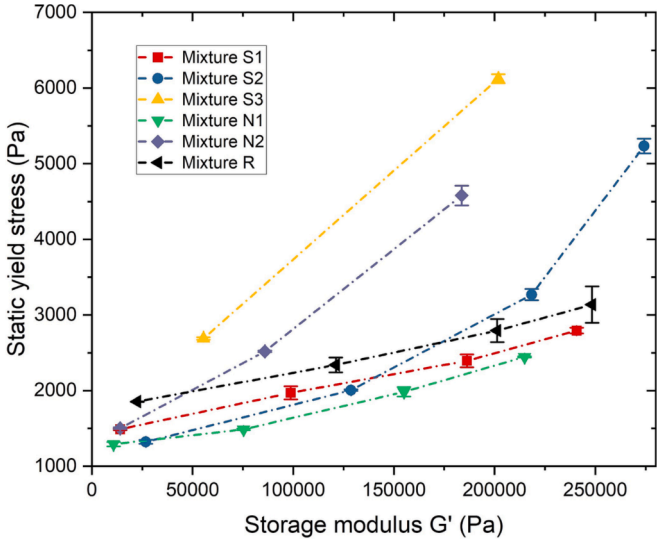

Fig. 15. The relationship between static yield stress from the CSR test and storage modulus *G'* from the SAOS test.

4.3. Potential use in 3DCP

Set-on-demand 3DCP (rheology and/or hydration control) has been reported as one of the most advanced and controllable printing strategies (see [15,16,93–95]). The strategy usually involves using a fresh mixture with great fluidity during the pumping process. The fresh mixture is delivered to the nozzle and mixed with an activator (or accelerator) only when the material is at the printhead [15]. In this study, we found that $CaCl_2$ solution can significantly accelerate structural build-up of LC3 mixture, making it a promising candidate to be used as an activator for set-on-demand printing. However, the concentration of the $CaCl_2$ solution should be optimized according to the composition of the LC3-based material (i.e., gypsum content) as well as specific printing requirements (e.g., printing speed, object size and geometry).

5. Conclusions

The main goal of the current study was to determine the effect of $CaCl_2$ and gypsum on the structural build-up and hydration characteristics of limestone-calcined clay-cement pastes within the first 75 min. Based on the results and discussions, the following findings can be summarized:

- The increase in storage modulus *G'* of the test samples based on the SAOS test can indicate the C-S-H growth and nucleation, which correlated well with the rise of chemically bound water content. However, except for C-S-H bridging, the static yield stress after 30 min seemed to be strongly influenced by the solid contact/friction between particles. A good inversely proportional correlation between static yield stress and the ratio of free water content to SSA_{total} was observed. The friction appeared to be dominated by the water film thickness (or particle distance) influenced by the free water amount, SSA_{total}, and voids between particles (also micropores/interlayer in calcined clay particles).
- Increasing the dosage of $CaCl_2$ can significantly accelerate the structuration and very early-age hydration of LC3 pastes, i.e., the acceleration of *G'* and static yield stress evolution with time, the increase in released reaction heat, chemically bound water content, crystal formation (portlandite, ettringite and Friedel's salt) and SSA_{total}.
- For the mixtures without $CaCl_2$, the increase of gypsum amount can slightly boost the development of *G'* and static yield stress with time, and increase the chemically bound water content and SSA_{total}. In addition, the acceleration of structuration and hydration may be related to the unreacted gypsum in the system, which seems to ease the inhibition of C_3S dissolution induced by aluminate ions (from calcined clay) and increase SSA_{total}.
- Compared to mixture N2 (2.4% $CaCl_2$ and no gypsum), mixture S2 (2.4% $CaCl_2$ and 2% gypsum) exhibited a faster *G'* evolution, a higher value of chemically bound water content and SSA_{total}, but a lower static yield stress at the same resting time which may be attributed to the absence of Friedel's salt.

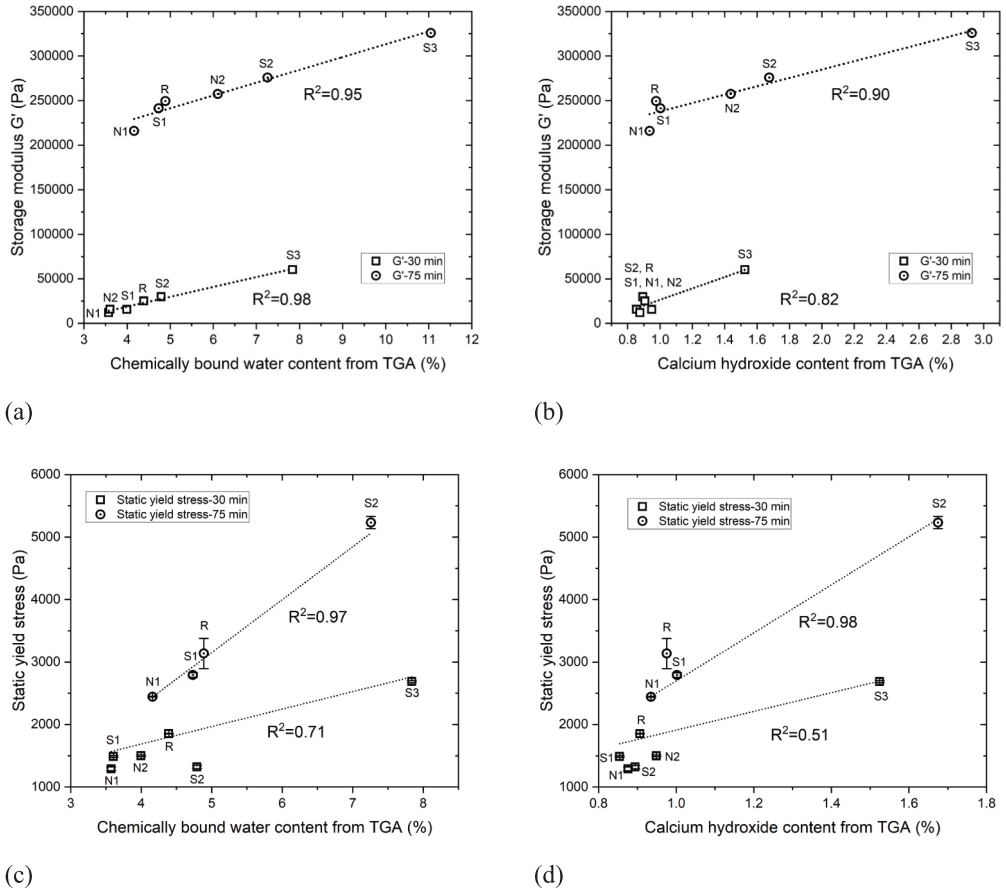

Fig. 16. Correlation between: (a) Storage modulus *G'* from the SAOS test and chemically bound water from the TGA at 30 min and 75 min; (b) Storage modulus *G'* from the SAOS test and calcium hydroxide from the TGA at 30 min and 75 min; (c) Static yield stress from the CSR test and chemically bound water from the TGA at 30 min and 75 min; (d) Static yield stress from the CSR test and calcium hydroxide from the TGA at 30 min and 75 min.

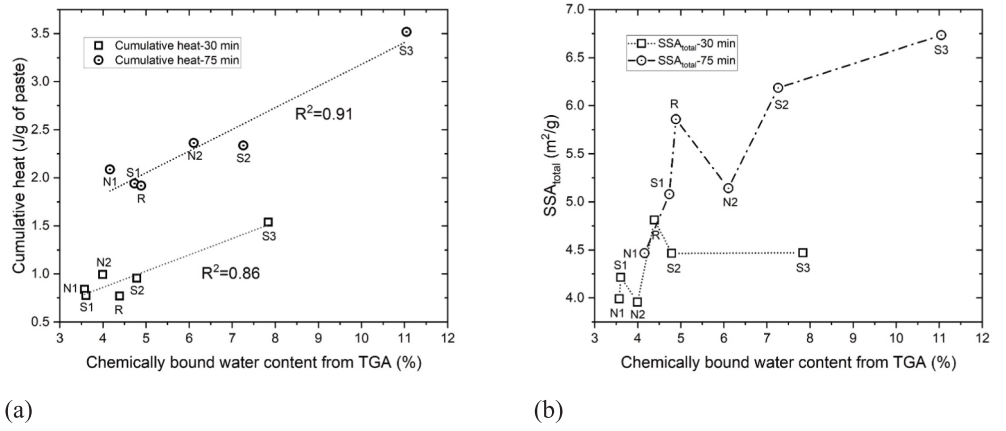

Fig. 17. Correlation between: (a) Cumulative heat and chemically bound water from the TGA at 30 min and 75 min; (b) SSA_{total} and chemically bound water from the TGA at 30 min and 75 min.

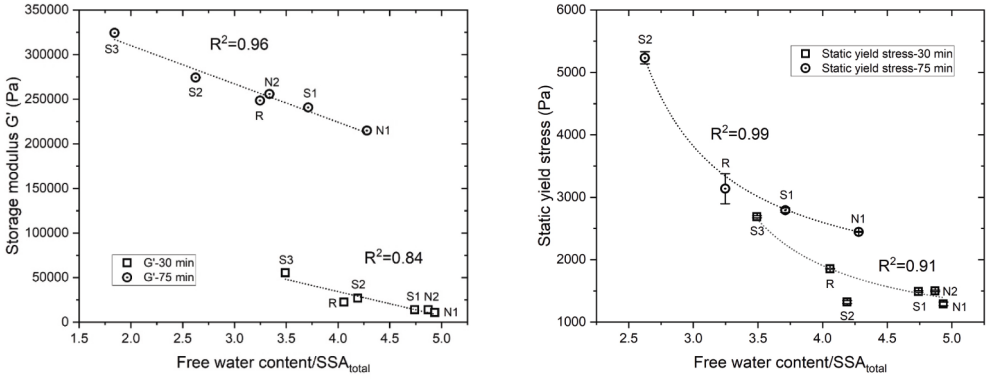

Fig. 18. Correlation between: (a) Storage modulus *G'* from the SAOS test and free water content/SSA_{total} at 30 min and 75 min; (b) Static yield stress from the CSR test and free water content/SSA_{total} at 30 min and 75 min. Free water content = Total water content + chemically bound water content from gypsum - Chemically bound water content (acquired from the TGA).

Declaration of Competing Interest

The authors declare that they have no known competing financial interests or personal relationships that could have appeared to influence the work reported in this paper.

Data availability

Data will be made available on request.

Acknowledgments

Yu Zhang and Xuhui Liang want to acknowledge the funding supported by China Scholarship Council under grant No. 201808320456, 201806050051. The authors wish to thank Mr. Arjan Thijssen and Mr. John van den Berg for their support in XRD and SSA measurement.

References

[1] M. Sharma, S. Bishnoi, F. Martirena, K. Scrivener, Limestone calcined clay cement and concrete: a state-of-the-art review, Cem. Concr. Res. 149 (2021), 106564, https://doi.org/10.1016/j.cemconres.2021.106564.
[2] F. Zunino, K. Scrivener, The influence of the filler effect on the sulfate requirement of blended cements, Cem. Concr. Res. 126 (2019), 105918, https://doi.org/10.1016/j.cemconres.2019.105918.
[3] K. Scrivener, F. Martirena, S. Bishnoi, S. Maity, Calcined clay limestone cements (LC3), Cem. Concr. Res. 114 (2018) 49–56, https://doi.org/10.1016/j.cemconres.2017.08.017.
[4] W. Huang, H. Kazemi-Kamyab, W. Sun, K. Scrivener, Effect of replacement of silica fume with calcined clay on the hydration and microstructural development of eco-UHPFRC, Mater. Des. 121 (2017) 36–46, https://doi.org/10.1016/j.matdes.2017.02.052.
[5] Z. Shi, M.R. Geiker, K. De Weerdt, T.A. Østnor, B. Lothenbach, F. Winnefeld, J. Skibsted, Role of calcium on chloride binding in hydrated Portland cement–metakaolin–limestone blends, Cem. Concr. Res. 95 (2017) 205–216, https://doi.org/10.1016/j.cemconres.2017.02.003.
[6] R. Hay, L. Li, K. Celik, Shrinkage, hydration, and strength development of limestone calcined clay cement (LC3) with different sulfation levels, Cem. Concr. Compos. 127 (2022), 104403, https://doi.org/10.1016/j.cemconcomp.2021.104403.
[7] S. Sánchez Berriel, A. Favier, E. Rosa Domínguez, I.R. Sánchez MacHado, U. Heierli, K. Scrivener, F. Martirena Hernández, G. Habert, Assessing the environmental and economic potential of Limestone Calcined Clay Cement in Cuba, J. Clean. Prod. 124 (2016) 361–369, https://doi.org/10.1016/j.jclepro.2016.02.125.
[8] Y. Chen, C.R. Rodriguez, Z. Li, B. Chen, O. Çopuroğlu, E. Schlangen, Effect of different grade levels of calcined clays on fresh and hardened properties of ternary-blended cementitious materials for 3D printing, Cem. Concr. Compos. 114 (2020), 103708, https://doi.org/10.1016/j.cemconcomp.2020.103708.
[9] Y. Chen, S. Chaves Figueiredo, Z. Li, Z. Chang, K. Jansen, O. Çopuroğlu, E. Schlangen, Improving printability of limestone-calcined clay-based cementitious materials by using viscosity-modifying admixture, Cem. Concr. Res. 132 (2020), 106040, https://doi.org/10.1016/j.cemconres.2020.106040.
[10] S. Bhattacherjee, A.S. Basavaraj, A.V. Rahul, M. Santhanam, R. Gettu, B. Panda, E. Schlangen, Y. Chen, O. Copuroglu, G. Ma, L. Wang, M.A. Basit Beigh, V. Mechtcherine, Sustainable materials for 3D concrete printing, Cem. Concr. Compos. 122 (2021), 104156, https://doi.org/10.1016/j.cemconcomp.2021.104156.
[11] Y. Chen, S. He, Y. Zhang, Z. Wan, O. Çopuroğlu, E. Schlangen, 3D printing of calcined clay-limestone-based cementitious materials, Cem. Concr. Res. 149 (2021), 106553, https://doi.org/10.1016/j.cemconres.2021.106553.
[12] Y. Chen, S. He, Y. Gan, O. Çopuroğlu, F. Veer, E. Schlangen, A review of printing strategies, sustainable cementitious materials and characterization methods in the context of extrusion-based 3D concrete printing, J. Build. Eng. 45 (2022), 103599, https://doi.org/10.1016/j.jobe.2021.103599.
[13] T.R. Muzenda, P. Hou, S. Kawashima, T. Sui, X. Cheng, The role of limestone and calcined clay on the rheological properties of LC3, Cem. Concr. Compos. 107 (2020), 103516, https://doi.org/10.1016/j.cemconcomp.2020.103516.
[14] M.A.B. Beigh, V.N. Nerella, E. Secrieru, V. Mechtcherine, Structural build-up behavior of limestone calcined clay cement (LC^3) pastes in the context of digital concrete construction ., in: Rheol. Process. Constr. Mater., 2019: pp. 1–8.
[15] L. Reiter, T. Wangler, A. Anton, R.J. Flatt, Setting on demand for digital concrete – Principles, measurements, chemistry, validation, Cem. Concr. Res. 132 (2020), 106047, https://doi.org/10.1016/j.cemconres.2020.106047.
[16] Y. Tao, A.V. Rahul, K. Lesage, Y. Yuan, K. Van Tittelboom, G. De Schutter, Stiffening control of cement-based materials using accelerators in inline mixing processes: Possibilities and challenges, Cem. Concr. Compos. 119 (2021), 103972, https://doi.org/10.1016/j.cemconcomp.2021.103972.
[17] P.C. Aïtcin, Accelerators, Sci. Technol. Concr. Admixtures. (2015) 405–413. https://doi.org/10.1016/B978-0-08-100693-1.00019-9.
[18] L. Steger, S. Blotevogel, L. Frouin, C. Patapy, M. Cyr, Experimental evidence for the acceleration of slag hydration in blended cements by the addition of CaCl2, Cem. Concr. Res. 149 (2021) 2–10, https://doi.org/10.1016/j.cemconres.2021.106558.
[19] K. Riding, D.A. Silva, K. Scrivener, Early age strength enhancement of blended cement systems by CaCl2 and diethanol-isopropanolamine, Cem. Concr. Res. 40 (2010) 935–946, https://doi.org/10.1016/j.cemconres.2010.01.008.
[20] B. Pacewska, I. Wilińska, G. Blonkowski, Investigations of cement early hydration in the presence of chemically activated fly ash: Use of calorimetry and infrared absorption methods, J. Therm. Anal. Calorim. 93 (2008) 769–776, https://doi.org/10.1007/s10973-008-9143-7.
[21] F. Bellmann, J. Stark, Activation of blast furnace slag by a new method, Cem. Concr. Res. 39 (2009) 644–650, https://doi.org/10.1016/j.cemconres.2009.05.012.
[22] N. Makaratat, C. Jaturapitakkul, C. Namarak, V. Sata, Effects of binder and CaCl2 contents on the strength of calcium carbide residue-fly ash concrete, Cem. Concr. Compos. 33 (2011) 436–443, https://doi.org/10.1016/j.cemconcomp.2010.12.004.
[23] A. Perrot, Y. Jacquet, D. Rangeard, E. Courteille, M. Sonebi, Nailing of layers: a promising way to reinforce concrete 3D printing structures, Materials (Basel). 13 (2020) 1518, https://doi.org/10.3390/ma13071518.
[24] T. Marchment, J. Sanjayan, Reinforcement method for 3D concrete printing using paste-coated bar penetrations, Autom. Constr. 127 (2021), 103694, https://doi.org/10.1016/j.autcon.2021.103694.
[25] A. Ahmed, S. Guo, Z. Zhang, C. Shi, D. Zhu, A review on durability of fiber reinforced polymer (FRP) bars reinforced seawater sea sand concrete, Constr. Build. Mater. 256 (2020), 119484, https://doi.org/10.1016/j.conbuildmat.2020.119484.

[26] B.T. Huang, J.Q. Wu, J. Yu, J.G. Dai, C.K.Y. Leung, V.C. Li, Seawater sea-sand engineered/strain-hardening cementitious composites (ECC/SHCC): Assessment and modeling of crack characteristics, Cem. Concr. Res. 140 (2021), 106292, https://doi.org/10.1016/j.cemconres.2020.106292.
[27] O. Kayali, M.S.H. Khan, M. Sharfuddin Ahmed, The role of hydrotalcite in chloride binding and corrosion protection in concretes with ground granulated blast furnace slag, Cem. Concr. Compos. 34 (2012) 936–945, https://doi.org/10.1016/j.cemconcomp.2012.04.009.
[28] P. Li, W. Li, Z. Sun, L. Shen, D. Sheng, Development of sustainable concrete incorporating seawater : A critical review on cement hydration, microstructure and mechanical strength, Cem. Concr. Compos. 121 (2021), 104100, https://doi.org/10.1016/j.cemconcomp.2021.104100.
[29] Z. Shi, Z. Shui, Q. Li, H. Geng, Combined effect of metakaolin and sea water on performance and microstructures of concrete, Constr. Build. Mater. 74 (2015) 57–64, https://doi.org/10.1016/j.conbuildmat.2014.10.023.
[30] Q. Li, H. Geng, Z. Shui, Y. Huang, Effect of metakaolin addition and seawater mixing on the properties and hydration of concrete, Appl. Clay Sci. 115 (2015) 51–60, https://doi.org/10.1016/j.clay.2015.06.043.
[31] M. Antoni, J. Rossen, F. Martirena, K. Scrivener, Cement substitution by a combination of metakaolin and limestone, Cem. Concr. Res. 42 (2012) 1579–1589, https://doi.org/10.1016/j.cemconres.2012.09.006.
[32] F. Avet, E. Boehm-Courjault, K. Scrivener, Investigation of C-A-S-H composition, morphology and density in Limestone Calcined Clay Cement (LC3), Cem. Concr. Res. 115 (2019) 70–79, https://doi.org/10.1016/j.cemconres.2018.10.011.
[33] J. Ston, A. Hilaire, K. Scrivener, Autogenous shrinkage and creep of limestone and calcined clay based binders, RILEM Bookseries. 16 (2018) 447–454. https://doi.org/10.1007/978-94-024-1207-9_72.
[34] K. Mehta, P.J.M. Monteiro, Concrete: Microstructure, Properties, and Materials, 3rd ed., McGraw-Hill, New York, 2006. https://doi.org/10.1036/0071462899.
[35] Y. Chen, F. Veer, O. Çopuroğlu, A critical review of 3D concrete printing as a low CO 2 concrete approach, Heron. 62 (2017) 167–194.
[36] A. Perrot, D. Rangeard, A. Pierre, Structural built-up of cement-based materials used for 3D-printing extrusion techniques, Mater. Struct. 49 (2016) 1213–1220, https://doi.org/10.1617/s11527-015-0571-0.
[37] Q. Yuan, D. Zhou, K.H. Khayat, D. Feys, C. Shi, On the measurement of evolution of structural build-up of cement paste with time by static yield stress test vs. small amplitude oscillatory shear test, Cem. Concr. Res. 99 (2017) 183–189, https://doi.org/10.1016/j.cemconres.2017.05.014.
[38] N. Roussel, G. Ovarlez, S. Garrault, C. Brumaud, The origins of thixotropy of fresh cement pastes, Cem. Concr. Res. 42 (2012) 148–157, https://doi.org/10.1016/j.cemconres.2011.09.004.
[39] J. Mewis, N.J. Wagner, Thixotropy, Adv. Colloid Interface Sci. 147–148 (2009) 214–227, https://doi.org/10.1016/j.cis.2008.09.005.
[40] N. Roussel, Rheological requirements for printable concretes, Cem. Concr. Res. 112 (2018) 76–85, https://doi.org/10.1016/j.cemconres.2018.04.005.
[41] N. Roussel, H. Bessaies-Bey, S. Kawashima, D. Marchon, K. Vasilic, R. Wolfs, Recent advances on yield stress and elasticity of fresh cement-based materials, Cem. Concr. Res. 124 (2019), 105798, https://doi.org/10.1016/j.cemconres.2019.105798.
[42] R.J.M. Wolfs, F.P. Bos, T.A.M. Salet, Early age mechanical behaviour of 3D printed concrete: Numerical modelling and experimental testing, Cem. Concr. Res. 106 (2018) 103–116, https://doi.org/10.1016/j.cemconres.2018.02.001.
[43] S. Ma, Y. Qian, S. Kawashima, Experimental and modeling study on the non-linear structural build-up of fresh cement pastes incorporating viscosity modifying admixtures, Cem. Concr. Res. 108 (2018) 1–9, https://doi.org/10.1016/j.cemconres.2018.02.022.
[44] D. Jiao, K. El Cheikh, C. Shi, K. Lesage, G. De Schutter, Structural build-up of cementitious paste with nano-Fe3O4 under time-varying magnetic fields, Cem. Concr. Res. 124 (2019) 105857.
[45] M.A. Moeini, M. Hosseinpoor, A. Yahia, Effectiveness of the rheometric methods to evaluate the build-up of cementitious mortars used for 3D printing, Constr. Build. Mater. 257 (2020), 119551, https://doi.org/10.1016/j.conbuildmat.2020.119551.
[46] V. Mechtcherine, F.P. Bos, A. Perrot, W.R.L. da Silva, V.N. Nerella, S. Fataei, R.J. M. Wolfs, M. Sonebi, N. Roussel, Extrusion-based additive manufacturing with cement-based materials – Production steps, processes, and their underlying physics: A review, Cem. Concr. Res. 132 (2020), 106037, https://doi.org/10.1016/j.cemconres.2020.106037.
[47] Y. Chen, C. Liu, R. Cao, C. Chen, V. Mechtcherine, Y. Zhang, Systematical investigation of rheological performance regarding 3D printing process for alkali-activated materials: Effect of precursor nature, Cem. Concr. Compos. 128 (2022), 104450, https://doi.org/10.1016/j.cemconcomp.2022.104450.
[48] A.V. Rahul, M. Santhanam, H. Meena, Z. Ghani, 3D printable concrete: Mixture design and test methods, Cem. Concr. Compos. 97 (2019) 13–23, https://doi.org/10.1016/j.cemconcomp.2018.12.014.
[49] M. Chen, B. Liu, L. Li, L. Cao, Y. Huang, S. Wang, P. Zhao, L. Lu, X. Cheng, Rheological parameters, thixotropy and creep of 3D-printed calcium sulfoaluminate cement composites modified by bentonite, Compos. Part B Eng. 186 (2020), 107821, https://doi.org/10.1016/j.compositesb.2020.107821.
[50] P.J. Kruger, S. Zeranka, G.P.A.G. van Zijl, An ab initio approach for thixotropic characterisation of nanoparticle-infused 3D printable concrete, Constr. Build Mater. (2019).
[51] F. Mahaut, S. Mokéddem, X. Chateau, N. Roussel, G. Ovarlez, Effect of coarse particle volume fraction on the yield stress and thixotropy of cementitious materials, Cem. Concr. Res. 38 (2008) 1276–1285, https://doi.org/10.1016/j.cemconres.2008.06.001.
[52] A. Perrot, T. Lecompte, P. Estellé, S. Amziane, Structural build-up of rigid fiber reinforced cement-based materials, Mater. Struct. Constr. 46 (2013) 1561–1568, https://doi.org/10.1617/s11527-012-9997-9.
[53] Y. Qian, S. Kawashima, Distinguishing dynamic and static yield stress of fresh cement mortars through thixotropy, Cem. Concr. Compos. 86 (2018) 288–296, https://doi.org/10.1016/j.cemconcomp.2017.11.019.
[54] Y. Qian, S. Kawashima, Use of creep recovery protocol to measure static yield stress and structural rebuilding of fresh cement pastes, Cem. Concr. Res. 90 (2016) 73–79, https://doi.org/10.1016/j.cemconres.2016.09.005.
[55] L.J. Struble, M.A. Schultz, Using creep and recovery to study flow behavior of fresh cement paste, Cem. Concr. Res. 23 (1993) 1369–1379, https://doi.org/10.1016/0008-8846(93)90074-J.
[56] J.J. Chen, A.K.H. Kwan, Superfine cement for improving packing density, rheology and strength of cement paste, Cem. Concr. Compos. 34 (2012) 1–10, https://doi.org/10.1016/j.cemconcomp.2011.09.006.
[57] W.W.S. Fung, A.K.H. Kwan, Role of water film thickness in rheology of CSF mortar, Cem. Concr. Compos. 32 (2010) 255–264, https://doi.org/10.1016/j.cemconcomp.2010.01.005.
[58] K. Vance, A. Kumar, G. Sant, N. Neithalath, The rheological properties of ternary binders containing Portland cement, limestone, and metakaolin or fly ash, Cem. Concr. Res. 52 (2013) 196–207, https://doi.org/10.1016/j.cemconres.2013.07.007.
[59] L.G. Li, X.Q. Chen, S.H. Chu, Y. Ouyang, A.K.H. Kwan, Seawater cement paste: Effects of seawater and roles of water film thickness and superplasticizer dosage, Constr. Build. Mater. 229 (2019) 116862.
[60] P. Nanthagopalan, M. Haist, M. Santhanam, H.S. Müller, Investigation on the influence of granular packing on the flow properties of cementitious suspensions, Cem. Concr. Compos. 30 (2008) 763–768, https://doi.org/10.1016/j.cemconcomp.2008.06.005.
[61] A.V. Rahul, A. Sharma, M. Santhanam, A desorptivity-based approach for the assessment of phase separation during extrusion of cementitious materials, Cem. Concr. Compos. 108 (2020), 103546, https://doi.org/10.1016/j.cemconcomp.2020.103546.
[62] V.N. Nerella, M.A.B. Beigh, S. Fataei, V. Mechtcherine, Strain-based approach for measuring structural build-up of cement pastes in the context of digital construction, Cem. Concr. Res. 115 (2019) 530–544, https://doi.org/10.1016/j.cemconres.2018.08.003.
[63] I. Ivanova, V. Mechtcherine, Possibilities and challenges of constant shear rate test for evaluation of structural build-up rate of cementitious materials, Cem. Concr. Res. 130 (2020), 105974, https://doi.org/10.1016/j.cemconres.2020.105974.
[64] Q. Yuan, X. Lu, K.H. Khayat, D. Feys, C. Shi, Small amplitude oscillatory shear technique to evaluate structural build-up of cement paste, Mater. Struct. Constr. 50 (2017) 1–12, https://doi.org/10.1617/s11527-016-0978-2.
[65] X. Dai, S. Aydın, M.Y. Yardımcı, K. Lesage, G. De Schutter, Effects of activator properties and GGBFS/FA ratio on the structural build-up and rheology of AAC, Cem. Concr. Res. 138 (2020), 106253, https://doi.org/10.1016/j.cemconres.2020.106253.
[66] X. Dai, S. Aydin, M. Yücel Yardimci, R.E.N. Qiang, K. Lesage, G. De Schutter, Rheology, early-age hydration and microstructure of alkali-activated GGBFS-Fly ash-limestone mixtures, Cem. Concr. Compos. 124 (2021), 104244, https://doi.org/10.1016/j.cemconcomp.2021.104244.
[67] B. Lothenbach, P. Durdzinski, K. De Weerdt, Thermogravimetric analysis, in: K. Scrivener, R. Snellings, B. Lothenbach (Eds.), A Pract. Guid. to Microstruct. Anal. Cem. Mater., CRC press, 2016: pp. 177–212.
[68] S. Mantellato, M. Palacios, R.J. Flatt, Relating early hydration, specific surface and flow loss of cement pastes, Mater. Struct. Constr. 52 (2019) 1–17, https://doi.org/10.1617/s11527-018-1304-y.
[69] G. Ovarlez, Introduction to the rheometry of complex suspensions, Woodhead Publishing Limited (2011), https://doi.org/10.1016/B978-0-85709-028-7.50002-9.
[70] S. Gauffinet-Garrault, The rheology of cement during setting, in: Underst. Rheol. Concr., Elsevier, 2012: pp. 96–113. https://doi.org/10.1533/9780857095282.1.96.
[71] T.G. Mezger, The Rheology Handbook, 4th ed., Emerald Group Publishing Limited, 2009. https://doi.org/10.1108/prt.2009.12938eac.006.
[72] X. Dai, S. Aydin, M.Y. Yardimci, K. Lesage, G. de Schutter, Influence of water to binder ratio on the rheology and structural Build-up of Alkali-Activated Slag/Fly ash mixtures, Constr. Build. Mater. 264 (2020), 120253, https://doi.org/10.1016/j.conbuildmat.2020.120253.
[73] M.K.D. Nicholas, M.G.J. Waters, K.M. Holford, G. Adusei, Analysis of rheological properties of bone cements, J. Mater. Sci. Mater. Med. 18 (2007) 1407–1412, https://doi.org/10.1007/s10856-007-0125-2.
[74] P. Steins, A. Poulesquen, O. Diat, F. Frizon, Structural evolution during geopolymerization from an early age to consolidated material, Langmuir. 28 (2012) 8502–8510, https://doi.org/10.1021/la300868v.
[75] D. Marchon, R.J. Flatt, Impact of chemical admixtures on cement hydration, Elsevier Ltd (2015), https://doi.org/10.1016/B978-0-08-100693-1.00012-6.
[76] A. Zingg, F. Winnefeld, L. Holzer, J. Pakusch, S. Becker, R. Figi, L. Gauckler, Interaction of polycarboxylate-based superplasticizers with cements containing different C3A amounts, Cem. Concr. Compos. 31 (2009) 153–162, https://doi.org/10.1016/j.cemconcomp.2009.01.005.
[77] P. Li, W. Li, T. Yu, F. Qu, V.W.Y. Tam, Investigation on early-age hydration, mechanical properties and microstructure of seawater sea sand cement mortar, Constr. Build. Mater. 249 (2020), 118776, https://doi.org/10.1016/j.conbuildmat.2020.118776.

[78] J. Liu, X. Fan, J. Liu, H. Jin, J. Zhu, W. Liu, Investigation on mechanical and micro properties of concrete incorporating seawater and sea sand in carbonized environment, Constr. Build. Mater. 307 (2021), 124986, https://doi.org/10.1016/j.conbuildmat.2021.124986.
[79] R. Roychand, S. De Silva, D. Law, S. Setunge, High volume fly ash cement composite modified with nano silica, hydrated lime and set accelerator, Mater. Struct. Constr. 49 (2016) 1997–2008, https://doi.org/10.1617/s11527-015-0629-z.
[80] F. Dalas, S. Pourchet, D. Rinaldi, A. Nonat, S. Sabio, M. Mosquet, Modification of the rate of formation and surface area of ettringite by polycarboxylate ether superplasticizers during early C3A-CaSO4 hydration, Cem. Concr. Res. 69 (2015) 105–113, https://doi.org/10.1016/j.cemconres.2014.12.007.
[81] Q. Yuan, D. Zhou, H. Huang, J. Peng, H. Yao, Structural build-up, hydration and strength development of cement-based materials with accelerators, Constr. Build. Mater. 259 (2020) 119775. https://doi.org/10.1016/j.conbuildmat.2020.119775.
[82] N. Shanahan, A. Sedaghat, A. Zayed, Effect of cement mineralogy on the effectiveness of chloride-based accelerator, Cem. Concr. Compos. 73 (2016) 226–234, https://doi.org/10.1016/j.cemconcomp.2016.07.015.
[83] M. Tramontin Souza, I. Maia Ferreira, E. Guzi de Moraes, L. Senff, S. Arcaro, J. R. Castro Pessôa, M.J. Ribeiro, A.P. Novaes de Oliveira, Role of chemical admixtures on 3D printed Portland cement: Assessing rheology and buildability, Constr. Build. Mater. 314 (2022), 125666, https://doi.org/10.1016/j.conbuildmat.2021.125666.
[84] M.D.A. Thomas, R.D. Hooton, A. Scott, H. Zibara, The effect of supplementary cementitious materials on chloride binding in hardened cement paste, Cem. Concr. Res. 42 (2012) 1–7, https://doi.org/10.1016/j.cemconres.2011.01.001.
[85] S. Sui, M. Wu, Z. Yang, F. Wang, Z. Liu, J. Jiang, An investigation on the formation of Friedel's salt in tricalcium silicate combined with metakaolin and limestone systems, Constr. Build. Mater. 284 (2021), 122855, https://doi.org/10.1016/j.conbuildmat.2021.122855.
[86] Y. Cao, L. Guo, B. Chen, J. Wu, Thermodynamic modelling and experimental investigation on chloride binding in cement exposed to chloride and chloride-sulfate solution, Constr. Build. Mater. 246 (2020), 118398, https://doi.org/10.1016/j.conbuildmat.2020.118398.
[87] K. De Weerdt, D. Orsáková, M.R. Geiker, The impact of sulphate and magnesium on chloride binding in Portland cement paste, Cem. Concr. Res. 65 (2014) 30–40, https://doi.org/10.1016/j.cemconres.2014.07.007.
[88] H. Hirao, K. Yamada, H. Takahashi, H. Zibara, Chloride binding of cement estimated by binding isotherms of hydrates, J. Adv. Concr. Technol. 3 (2005) 77–84, https://doi.org/10.3151/jact.3.77.
[89] J. Lapeyre, A. Kumar, Influence of pozzolanic additives on hydration mechanisms of tricalcium silicate, J. Am. Ceram. Soc. 101 (2018) 3557–3574, https://doi.org/10.1111/jace.15518.
[90] E. Pustovgar, R.K. Mishra, M. Palacios, J.B. d'Espinose de Lacaillerie, T. Matschei, A.S. Andreev, H. Heinz, R. Verel, R.J. Flatt, Influence of aluminates on the hydration kinetics of tricalcium silicate, Cem. Concr. Res. 100 (2017) 245–262, https://doi.org/10.1016/j.cemconres.2017.06.006.
[91] J. Skibsted, R. Snellings, Reactivity of supplementary cementitious materials (SCMs) in cement blends, Cem. Concr. Res. 124 (2019), 105799, https://doi.org/10.1016/j.cemconres.2019.105799.
[92] F. Zunino, K. Scrivener, Factors influencing the sulfate balance in pure phase C3S/C3A systems, Cem. Concr. Res. 133 (2020), 106085, https://doi.org/10.1016/j.cemconres.2020.106085.
[93] C. Gosselin, R. Duballet, P. Roux, N. Gaudillière, J. Dirrenberger, P. Morel, Large-scale 3D printing of ultra-high performance concrete - a new processing route for architects and builders, Mater. Des. 100 (2016) 102–109, https://doi.org/10.1016/j.matdes.2016.03.097.
[94] L. Reiter, T. Wangler, N. Roussel, R.J. Flatt, The role of early age structural build-up in digital fabrication with concrete, Cem. Concr. Res. 112 (2018) 86–95, https://doi.org/10.1016/j.cemconres.2018.05.011.
[95] V. Esnault, A. Labyad, M. Chantin, F. Toussaint, Experience in Online Modification of Rheology and Strength Acquisition of 3D Printable Mortars, in: T. Wangler, R. Flatt (Eds.), First RILEM Int. Conf. Concr. Digit. Fabr. – Digit. Concr., Springer International Publishing, 2019: pp. 24–38. https://doi.org/10.1007/978-3-319-99519-9_3.